Title

Insights into the pathogenesis of dominant retinitis pigmentosa associated with a D477G mutation in RPE65.

Journal

Human Molecular Genetics, 27(13)

Authors

Choi, Elliot
Suh, Susie
Sander, Christopher
et al.

Publication Date

2018-07-01

DOI

10.1093/hmg/ddy128

Peer reviewed

Human Molecular Genetics, 2018, Vol. 27, No. 13 2225–2243

doi: 10.1093/hmg/ddy128
Advance Access Publication Date: 12 April 2018
Original Article

ORIGINAL ARTICLE

Insights into the pathogenesis of dominant retinitis pigmentosa associated with a D477G mutation in RPE65

Elliot H. Choi[1], Susie Suh[1], Christopher L. Sander[1], Christian J. Ortiz Hernandez[1,2], Elizabeth R. Bulman[1,3], Nimesh Khadka[1], Zhiqian Dong[1,4], Wuxian Shi[5], Krzysztof Palczewski[1,6,*] and Philip D. Kiser[1,3,6,*]

[1]Department of Pharmacology, School of Medicine, Case Western Reserve University, Cleveland, OH 44106, USA, [2]University of Puerto Rico at Humacao, Humacao, PR, USA, [3]Research Service, Louis Stokes Cleveland VA Medical Center, Cleveland, OH 44106, USA, [4]Polgenix Inc., Cleveland, OH 44106, USA, [5]National Synchrotron Light Source-II, Brookhaven National Laboratory, Upton, NY 11973, USA and [6]Cleveland Center for Membrane and Structural Biology, Case Western Reserve University, Cleveland, OH 44106, USA

*To whom correspondence should be addressed at: Department of Pharmacology, School of Medicine, Case Western Reserve University, 10900 Euclid Ave., Cleveland, OH 44106-4965, USA. Tel: +1 2163684631; Fax: +1 2163681300; Email: kxp65@case.edu (K.P.); Department of Pharmacology, School of Medicine, Case Western Reserve University, 10900 Euclid Ave., Cleveland, OH 44106-4965, USA. Tel: +1 2163680040; Fax: +1 2163681300; Email: pdk7@case.edu (P.D.K.)

Abstract

RPE65 is the essential *trans–cis* isomerase of the classical retinoid (visual) cycle. Mutations in *RPE65* give rise to severe retinal dystrophies, most of which are associated with loss of protein function and recessive inheritance. The only known exception is a c.1430G>A (D477G) mutation that gives rise to dominant retinitis pigmentosa with delayed onset and choroidal and macular involvement. Position 477 is distant from functionally critical regions of RPE65. Hence, the mechanism of D477G pathogenicity remains unclear, although protein misfolding and aggregation mechanisms have been suggested. We characterized a D477G knock-in mouse model which exhibited mild age-dependent changes in retinal structure and function. Immunoblot analysis of protein extracts from the eyes of these knock-in mice demonstrated the presence of ubiquitinated RPE65 and reduced RPE65 expression. We observed an accumulation of retinyl esters in the knock-in mice as well as a delay in rhodopsin regeneration kinetics and diminished electroretinography responses, indicative of RPE65 functional impairment induced by the D477G mutation *in vivo*. However, a cell line expressing D477G RPE65 revealed protein expression levels, cellular localization and retinoid isomerase activity comparable to cells expressing wild-type protein. Structural analysis of an RPE65 chimera suggested that the D477G mutation does not perturb protein folding or tertiary structure. Instead, the mutation generates an aggregation-prone surface that could induce cellular toxicity through abnormal complex formation as suggested by crystal packing analysis. These results indicate that a toxic gain-of-function induced by the D477G RPE65 substitution may play a role in the pathogenesis of this form of dominant retinitis pigmentosa.

Received: February 28, 2018. **Revised:** April 2, 2018. **Accepted:** April 6, 2018

Introduction

The retinoid (visual) cycle is an enzymatic pathway that regenerates visual chromophore in vertebrates. This metabolic cycle takes place mainly in the retinal pigment epithelium (RPE), a single layer of cells adjacent to the photoreceptor outer segments. Continuous regeneration of visual chromophore is critical for detection of light, and defects in the enzymes involved in the retinoid cycle often culminate in retinal dystrophy. One of the indispensable enzymes of the visual cycle is an RPE-specific protein known as RPE65, which is the retinoid isomerase that catalyzes cleavage and isomerization of all-*trans*-retinyl esters to form 11-*cis*-retinol (1–3).

RPE65 is a 61 kDa protein bound to the endoplasmic reticulum (ER) membranes of the RPE that is highly conserved among vertebrates and belongs to the carotenoid cleavage oxygenase (CCO) enzyme family (4–7). To date, over 100 mutations in *RPE65* have been implicated in Leber congenital amaurosis (LCA) and retinitis pigmentosa (RP) (8), and almost all of these are inherited in a recessive manner. However, an autosomal dominant form of RPE65-associated RP with choroidal involvement has also been identified (9,10). This novel form of RP arises from a missense mutation in exon 13 of *RPE65* (c.1430G>A) that changes the amino acid residue encoded at position 477 from Asp to Gly (D477G).

Carriers of the D477G mutation exhibit varying phenotypes including disease severity and age of disease onset. They also display areas of retinal atrophy ranging from the choroid to the photoreceptor layer (9,10). Unlike typical RP patients who present with progressive visual field loss from the mid to far periphery, most carriers of the D477G mutation initially present with a central visual defect (10). Moreover, choroidal atrophy and RPE hypertrophy are frequently observed and distinctive features associated with this mutation (9,10).

Previous studies of the RPE65 D477G mutation have suggested that the pathological phenotype is attributable to structural destabilization of RPE65 due to increased folding free energy (9) and delayed chromophore regeneration resulting from dominant-negative suppression of RPE65 retinoid isomerase activity (11). However, visual cycle activity in heterozygous D477G knock-in (KI) mice can replenish sufficient 11-*cis*-retinaldehyde to support relatively normal retinal function (11). The disease-associated phenotypes in homozygous KI mice have not been reported to date, so the precise classification of this point mutation remains unclear. Understanding the pathological consequences of this mutation is likely to aid in the development of treatment strategies for this and potentially other RPE65-associated dominant forms of RP. For example, dominant-negative or haploinsufficiency mechanisms would imply that *RPE65* gene therapy may be of value to D477G subjects (12) whereas gain-of-function mechanisms would likely not be responsive to this intervention.

In this study, we assessed the phenotype of an independently-generated D477G mouse line in both the heterozygous and homozygous states using a combination of high-resolution imaging, histology, electroretinography (ERG) and retinoid profile analyses. We further studied the consequences of this mutation at the molecular level with *in vitro* isomerization assays, RNA sequencing, immunoblotting of ubiquitinated RPE65 and X-ray crystallographic analyses. These comprehensive studies provide novel insights into the pathogenesis of the D477G mutation.

Results

The D477G mutation does not affect expression, subcellular localization and isomerization activity *in vitro*

To evaluate the intracellular localization and enzymatic function of RPE65 carrying the D477G mutation, we used retroviral transduction to generate two NIH3T3 cell lines that stably express either LRAT that generates substrate for the isomerase and human RPE65 (hRPE65) or LRAT and the hRPE65 D477G mutant. Immunoblotting analysis of the cell lines showed comparable expression levels of hRPE65 and the D477G mutant (Fig. 1A), which differs from R91W, G244V and Y368H substitutions that cause decreased stability of RPE65 *in vitro* (13,14). Next, we examined whether the D477G mutant was properly localized within NIH3T3 cells. Immunofluorescence confocal microscopy revealed that hRPE65 co-localized with the ER marker calnexin, consistent with previous reports (4,5,15) (Fig. 1B). This localization was unchanged for D477G RPE65 suggesting the mutation does not affect protein trafficking or membrane association in this heterologous expression system (Fig. 1B). Our results cannot definitively exclude the possibility that protein is misfolded and retained in the ER. However, it would be expected that such a protein would be quickly degraded. Moreover, previous work has shown that aggregates of mutant RPE65 including L22P, T101I and L408P point mutants exhibited punctate-like inclusion bodies whereas wild-type (WT) RPE65 exhibited a homogenous ER distribution (16). Next, we assessed whether the D477G mutation changes RPE65 isomerization activity by incubating the NIH3T3 cell lines stably expressing LRAT and the D477G mutant or WT RPE65 protein with 10 μM all-*trans*-retinol for 16 h. Analysis of retinoids extracted from these cells revealed comparable production of 11-*cis*-retinol between the two cell lines (Fig. 1C–E). These findings suggest that the D477G mutation does not affect ER localization and isomerization activity of RPE65 in cell culture assays.

mRNA from D477G RPE65 and ubiquitination of RPE65 induced by the D477G mutation

We generated D477G RPE65 KI mice by replacing the endogenous *RPE65* gene with a targeting vector including exons 8–14 along with the D477G mutation (Fig. 2A). A neomycin (Neo) cassette flanked by Flp-recombinase target (FRT) sites was used for clonal selection and later excised by FLP recombinase expressed in the embryonic stem cells. The embryonic stem cells carrying the Neo deleted targeting vector were microinjected into C57Bl/6 blastocysts. The final KI allele contained the D477G mutation with one 85-bp FRT site remaining between exons 13 and 14. A primer set flanking the FRT site was used to distinguish the WT allele and mutant allele. WT mice had a 495-bp PCR product, whereas homozygous mice had a 580-bp PCR product; heterozygous mice had both PCR products (Fig. 2B). Additional sequencing of cDNA from the heterozygous mice showed transcription of both WT and D477G mRNA (Fig. 2C).

Next, we examined whether the D477G mutation affected the transcriptional level of RPE65 using real-time PCR. RPE65 mRNA levels were comparable between WT, heterozygous and homozygous KI mice (Supplementary Material, Fig. S1) consistent with prior data (11). To evaluate the ratio of transcribed WT and D477G mRNA, we collected 95 RPE65 cDNA clones from the RPE layer of heterozygous mice and sequenced them.

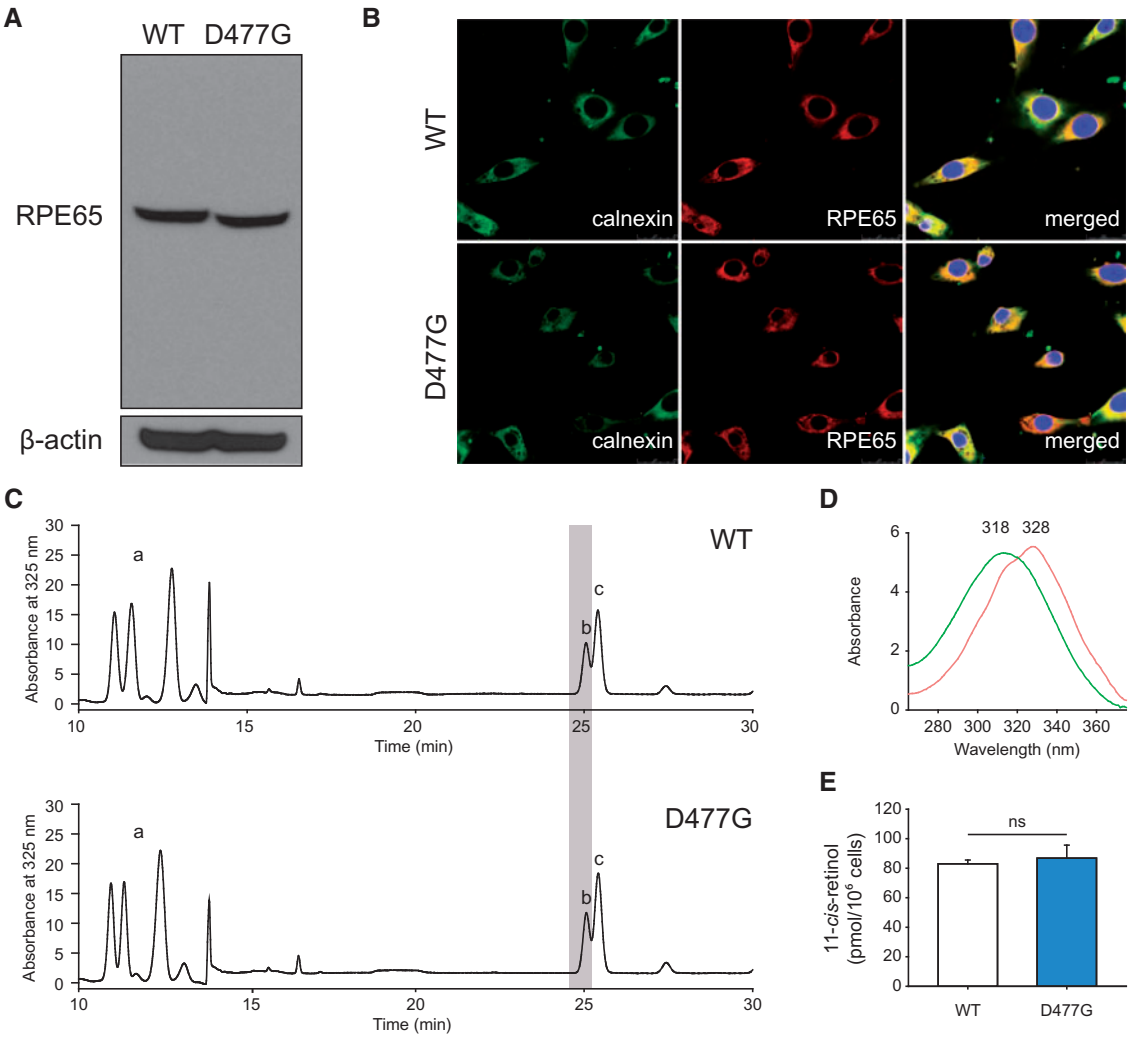

Figure 1. Analysis of NIH3T3 cells expressing LRAT and WT hRPE65 or D477G hRPE65. (**A**) Immunoblot of NIH3T3-LRAT-WT hRPE65 and NIH3T3-LRAT-D477G hRPE65 cells. Sample loading was normalized based on the signal for β-actin. (**B**) Subcellular localization of hRPE65 and D477G hRPE65. The merged images show the co-localization of hRPE65 or D477G RPE65 with the ER marker (calnexin). (**C**) HPLC analysis of retinoids extracted from NIH3T3 cells expressing LRAT and WT hRPE65 or D477G hRPE65. Chromatography peaks were identified based on elution time and their characteristic UV/vis absorbance spectra. Peaks 'a' correspond to retinyl esters, peaks 'b' correspond to 11-*cis*-retinol and peaks 'c' correspond to 13-*cis*-retinol. (**D**) UV/vis spectra of peaks 'b' (green) and 'c' (red) confirming their identities as 11-*cis*-retinol and 13-*cis*-retinol, respectively, by the characteristic spectral shapes and maximal absorbance wavelengths. (**E**) Quantification of the HPLC results presented in (**C**). $n = 3$. Data are shown as means ± S.E.M.

Importantly, the number of D477G clones was 3.75-fold less than that of WT clones (Table 1). We note that small differences in the mRNA secondary structure arising from the single nucleotide change could potentially bias the outcome of RT-PCR for the mutant transcript.

Next, we examined whether the D477G mutation affects translation or susceptibility of the protein to degradation. Immunoblotting of RPE lysates revealed that levels of RPE65 expression were decreased in heterozygous and to a greater extent in homozygous KI mice (Fig. 3A). Previous studies have shown degradation of RPE65 mutants via the ubiquitin-proteasome pathway *in vitro* and *in vivo* (17–19). To examine possible ubiquitination of RPE65 induced by the D477G substitution, we immunoprecipitated ubiquitinated proteins and then probed for the presence of RPE65 by immunoblotting. Lysates from WT mice did not exhibit ubiquitinated RPE65, whereas lysates from heterozygous and homozygous KI mice showed two distinct bands of increased molecular weight (Fig. 3B). These findings suggest that the D477G mutation facilitated mono- and di-ubiquitination of RPE65 *in vivo*.

Changes in retinal morphology associated with the D477G mutation

To assess the consequences of the D477G mutation on retinal morphology, we compared WT, heterozygous and homozygous KI mice at different ages ranging from 3 to 9 months. First, we used scanning laser ophthalmoscopy (SLO) with an excitation wavelength of 490 nm and an emission filter of 500–700 nm to visualize the retinal fundus. Autofluorescent spots were present in 9-month-old heterozygous and 6-month-old homozygous KI mice (Fig. 4). No such spots were observed in age-matched WT mice. This may represent inflammatory responses in the retina through activation of Müller cells, macrophages or microglia cells which were observed in several animal models displaying retinal degeneration (20–23). Next, we performed optical coherence tomography (OCT) imaging to visualize the retina in cross-section allowing us to determine whether the D477G mutation leads to retinal degeneration. A subtle reduction in outer nuclear layer (ONL) thickness was

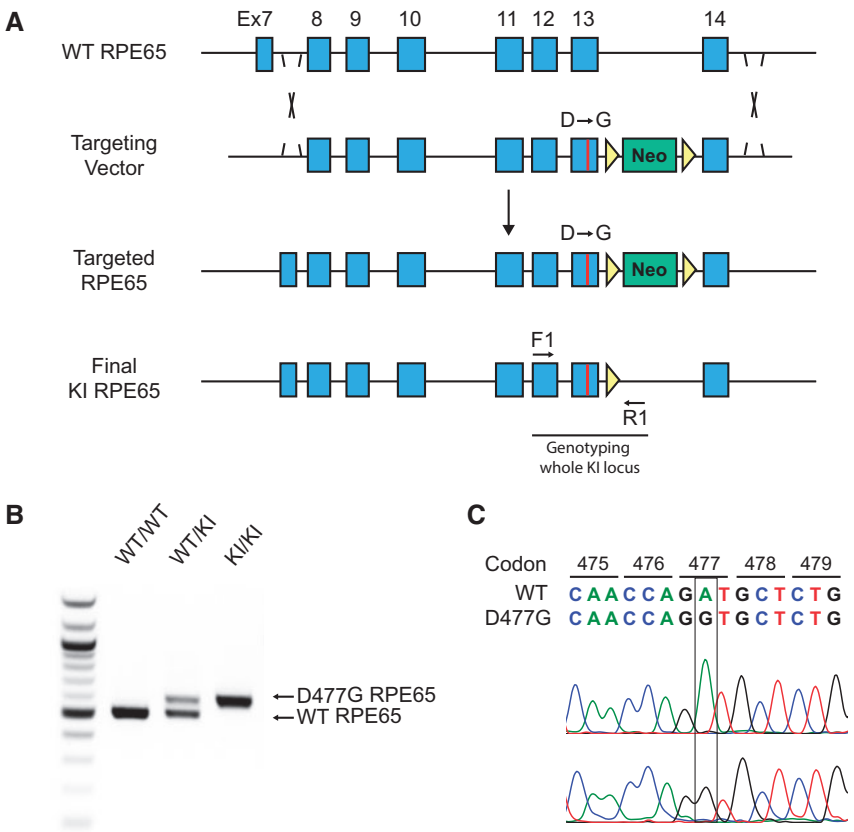

Figure 2. Targeting strategy used to generate D477G KI mice and molecular characterization. (**A**) D477G KI mice were generated by homologous recombination with an 11.3 kb targeting vector containing the FRT-flanked Neo cassette between exons 13 and 14. Codon 477 in exon 13 was changed from GAT to GGT. This change results in a D to G amino acid substitution. The FRT-flanked Neo cassette was deleted by FRT-FLP recombination to generate D477G RPE65 KI mice. The mouse retained an 85-bp FRT site in the intron between exons 13 and 14. (**B**) PCR primers flanking the FRT site, as shown in the bottom scheme of (A), were used for genotyping. The WT allele and D477G KI allele produced 495- and 580-bp PCR products, respectively. (**C**) Sequencing chromatograms of two RPE65 cDNA clones from the RPE of a 3-month-old heterozygous KI mouse confirmed the presence of both WT and mutant mRNAs. F, forward; R, reverse; KI, knock-in; WT, wild-type.

Table 1. cDNA ratio of D477G RPE65 to WT RPE65 revealed a decrease in mRNAs transcribed from RPE65 (c.1430G>A)

Mouse ID	No. of WT clones	No. of D477G clones
1	41	7
2	34	13
Total	75	20

observed in 6-month-old heterozygous and homozygous KI mice and this thinning became more prominent in 9-month-old heterozygous and homozygous KI mice compared with age-matched WT mice (Fig. 5A and B). Taken together, these results indicate the D477G mutation is associated with a slow degeneration that becomes more evident with aging. This finding is consistent with the phenotype observed in human patients harboring the same mutation.

Reduction in scotopic ERG responses associated with the D477G mutation

A previous study of the *D477G* mutation reported that rod ERG responses in patients harboring the mutation were impaired, even in individuals with mild structural abnormalities (9). To determine whether *D477G* affects the functional integrity of mouse retina and the rod photoreceptors in particular, we performed dark-adapted (scotopic) ERG recordings in both heterozygous and homozygous KI mice at 3, 6 and 9 months of age. ERG analysis in mice did not reveal a significant difference in a- and b-wave amplitudes between WT, heterozygous and homozygous KI mice up to 6-months of age. However, at 9-months of age, scotopic a- and b-wave responses in both heterozygous and homozygous KI mice declined compared with the corresponding responses in WT mice (Fig. 6A and B and Supplementary Material, Fig. S2A). Similar results were obtained for photopic a- and b-wave amplitudes (Fig. 6C and D and Supplementary Material, Fig. S2B). This result is consistent with the progressive thinning of the ONL in heterozygous and homozygous KI mice observed by OCT imaging and the later age of onset in humans with the D477G mutation compared with those with RPE65-associated recessive RP.

Impact of the D477G mutation on the mouse retinoid cycle

Animal models carrying P25L, R91W and L450M mutations in RPE65 have demonstrated delayed visual chromophore

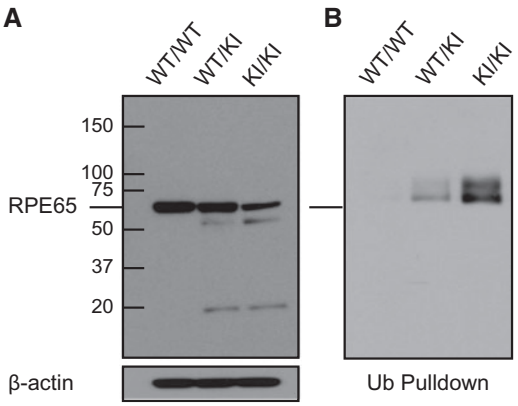

Figure 3. Decreased RPE65 protein level and ubiquitination of RPE65 in D477G KI mice. (**A**) RPE lysates from wild-type (WT/WT), heterozygous (WT/KI) and homozygous (KI/KI) mice were subjected to immunoblotting using an in-house generated RPE65 antibody. Equal protein sample loading was verified by β-actin immunoblotting. Note the slight reduction in RPE65 protein levels in the WT/KI sample and more substantial reduction in the KI/KI sample. Lower molecular weight bands recognized by the RPE65 antibody were present in the WT/KI and KI/KI samples but not WT/WT samples suggesting an elevated susceptibility to proteolysis induced by the D477G substitution. (**B**) RPE lysates from WT/WT, WT/KI and KI/KI mice were subjected to immunoprecipitation with a ubiquitin antibody followed by immunoblotting with RPE65 antibody. Ubiquitinated RPE65 was present in WT/KI and to a greater extent KI/KI samples whereas in the WT/WT sample it was scarcely detectable. This finding suggests that proteolysis could play a role in the reduced RPE65 levels observed in the KI mice.

regeneration (18,24,25). Therefore, we examined whether the D477G mutation perturbs the visual cycle. We analyzed the retinoid composition in dark-adapted WT, heterozygous and homozygous KI mice at different ages ranging from 1 to 3 months. The amount of 11-*cis*-retinal in heterozygous and homozygous KI mice did not differ from WT mice, whereas the amount of retinyl esters in heterozygous and homozygous KI mice was higher than that in WT mice (Fig. 7A–C). This elevated level of retinyl esters could be due to a feedback response to aberrant mutant protein. RPE65 could also play a role in retinyl ester mobilization from lipid droplet stores (retinosomes) (26,27) outside of its role in cleaving and isomerizing retinyl esters for visual chromophore production as recently suggested (28).

Next, we examined the amount of 11-*cis*-retinal in WT, heterozygous and homozygous KI mice dark adapted for 4, 8, 12 and 20 h following a 10 min bleach. Compared with WT mice, homozygous KI mice had significantly lower amounts of 11-*cis*-retinal after 4 and 8 h of dark adaptation; however, the amounts became comparable with those of WT mice after 20 h of dark adaptation (Fig. 7D). Heterozygous KI mice had significantly lower amounts of 11-*cis*-retinal after 4 h of dark adaptation, but levels became comparable with WT mice at 8 h of dark adaptation. This result was further supported by the elevated quantity of retinyl esters found in homozygous (and at some time points, heterozygous) KI mice (Fig. 7E). Additionally, we assessed the regeneration of 11-*cis*-retinal with the shorter dark-adaption period. WT, heterozygous and homozygous KI mice were exposed to a 10 min bleach, followed by dark adaptation for 10 min. As

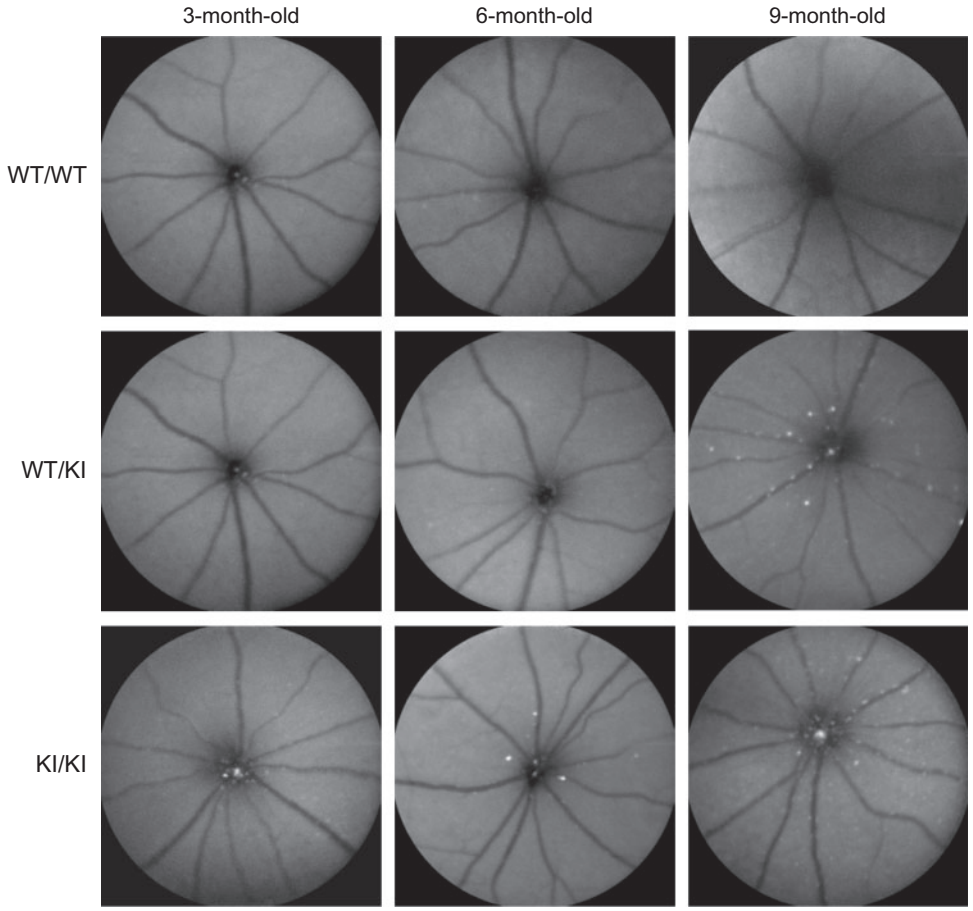

Figure 4. Fundus autofluorescent spots in D477G KI mice. Representative SLO fundus images from wild-type (WT/WT), heterozygous (WT/KI) and homozygous (KI/KI) mice at 3, 6 and 9 months of age. Autofluorescent spots were first noted in 9-month-old heterozygous and 6-month-old homozygous KI mice fundus images, whereas such spots were scarcely visible in the WT/WT fundus.

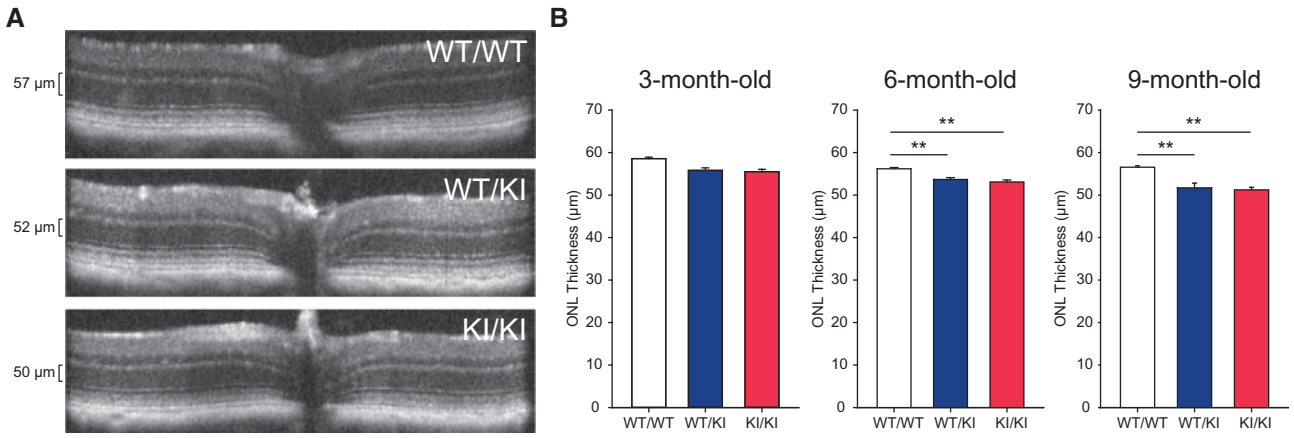

Figure 5. Retinal degeneration in D477G KI mice over time. (**A**) Representative OCT images of retinae crossing the optic nerve head from wild-type (WT/WT), heterozygous (WT/KI) and homozygous (KI/KI) mice at 9 months of age. Heterozygous and homozygous retinae displayed decreased thickness of the ONL (indicated by the brackets) compared with age-matched wild-type retina. (**B**) ONL layer thickness in wild-type (WT/WT), heterozygous (WT/KI) and homozygous (KI/KI) mice at 3, 6 and 9 months of age as measured by OCT. Both heterozygous and homozygous mice underwent mild progressive photoreceptor degeneration. $n = 4$–5 for the WT/WT group, $n = 5$ for the WT/KI group, $n = 5$ for the KI/KI group. ** indicates $P < 0.01$. Data are shown as mean ± S.E.M.

expected, levels of 11-*cis*-retinal were lower in heterozygous and homozygous mice compared to WT (Fig. 7F). This result was further supported by the elevated levels of retinyl esters found in heterozygous and homozygous KI mice (Fig. 7G). Taken together, this retinoid profile suggests the 11-*cis*-retinal regeneration rate was reduced in both heterozygous and homozygous KI mice.

Analysis of the D477 structural environment

To better understand the pathogenicity of the D477G substitution, we analyzed the structure of the region of the RPE65 sequence near this position. Asp is conserved at position 477 in RPE65 from primates to sea lamprey, consistent with an important role for this residue (Fig. 8A). The ExAC database revealed no missense mutations at position 477 although a synonymous substitution was documented (29). Interestingly, glycine is found at a position equivalent to position 477 of human RPE65 in some CCO enzymes including human BCO1 and BCO2 as well as *Synechocystis* ACO, indicating that Gly is tolerated for protein structure and function in the presence of a suitable surrounding sequence (Fig. 8A). The D477-containing loop and nearby residues in the surrounding β−strands are relatively well conserved between RPE65 and ACO compared with the protein chains as a whole, which exhibited only ∼25% sequence identity.

D477 occupies the n + 2 position of a type-1 β-turn element found within a loop connecting strands 32 and 33 of the β-propeller fold (30). Our inspection of known RPE65 crystal structures revealed a consistent secondary structure for this protein region with some rigid body variation in its overall position. This loop is located distant from the active site, does not contribute to the membrane binding surface of the enzyme and is not involved in formation of the conserved dimeric interface or any other protein–protein interaction preserved across known crystal structures of RPE65 (Fig. 8B) (31,32). Hence, a critical structural or functional role for D477 is not obvious from its position within the context of the three-dimensional structure. However, β−turns are known to exert pivotal roles in protein folding (33) and in protein–protein interactions (34). Thus, the D477G substitution could perturb the normal structure of this β−turn causing pathogenic protein misfolding as discussed previously (9,11). For example, a glycyl residue in the $n + 2$ position of the β−turn could promote switching to a type-II conformation (34), thereby promoting the above-mentioned effects. Indeed, inspection of PDB entries containing the "HPGA" sequence within a β−turn motif revealed that most are in a type-II conformation (35). β−turns with an "HPGA" sequence were observed only in non-metazoan species and are less common than the turns comprised of "HPDA" and "RPGG" sequences found in RPE65 and ACO, respectively.

Design and expression of a chimeric ACO protein containing the D477 loop

To date, it has not proven feasible to crystallize recombinantly produced RPE65, hampering direct examination of amino acid substitution effects on RPE65 structure. To circumvent this difficulty, we exploited the high structural similarity between RPE65 and ACO near position 477 (Fig. 8C) to design a chimeric protein in which residues 474–485 of RPE65 were replaced in the equivalent position of the ACO sequence (Fig. 8A). We also swapped four other residues in the ACO sequence to their RPE65 counterparts to maintain important chemical interactions and avoid steric clashes (Fig. 8A). We expressed this hybrid protein, referred to herein as "ACO/RPE65–477-loop," and its corresponding D477G mutant in *E. coli* using the procedure previously described for WT ACO (36). The two hybrid proteins were expressed in the soluble fraction at levels comparable with WT ACO (Fig. 9A, left) and could also be purified by the same protocol with a similar yield as ACO (Fig. 9A, right and Fig. 9B). All three enzymes also possessed comparable catalytic activities (Fig. 9C and Supplementary Material, Fig. S3). Given that the D477 loop is structurally isolated (Fig. 8B) we expected that sequence differences outside of this loop would have minimal impact on the potential influence of the D477G substitution on protein folding in either RPE65 or ACO/RPE65–477-loop. Based on this assumption, these results indicate that the D477G substitution does not have a marked effect on protein folding, which is consistent with the *in vitro* data we

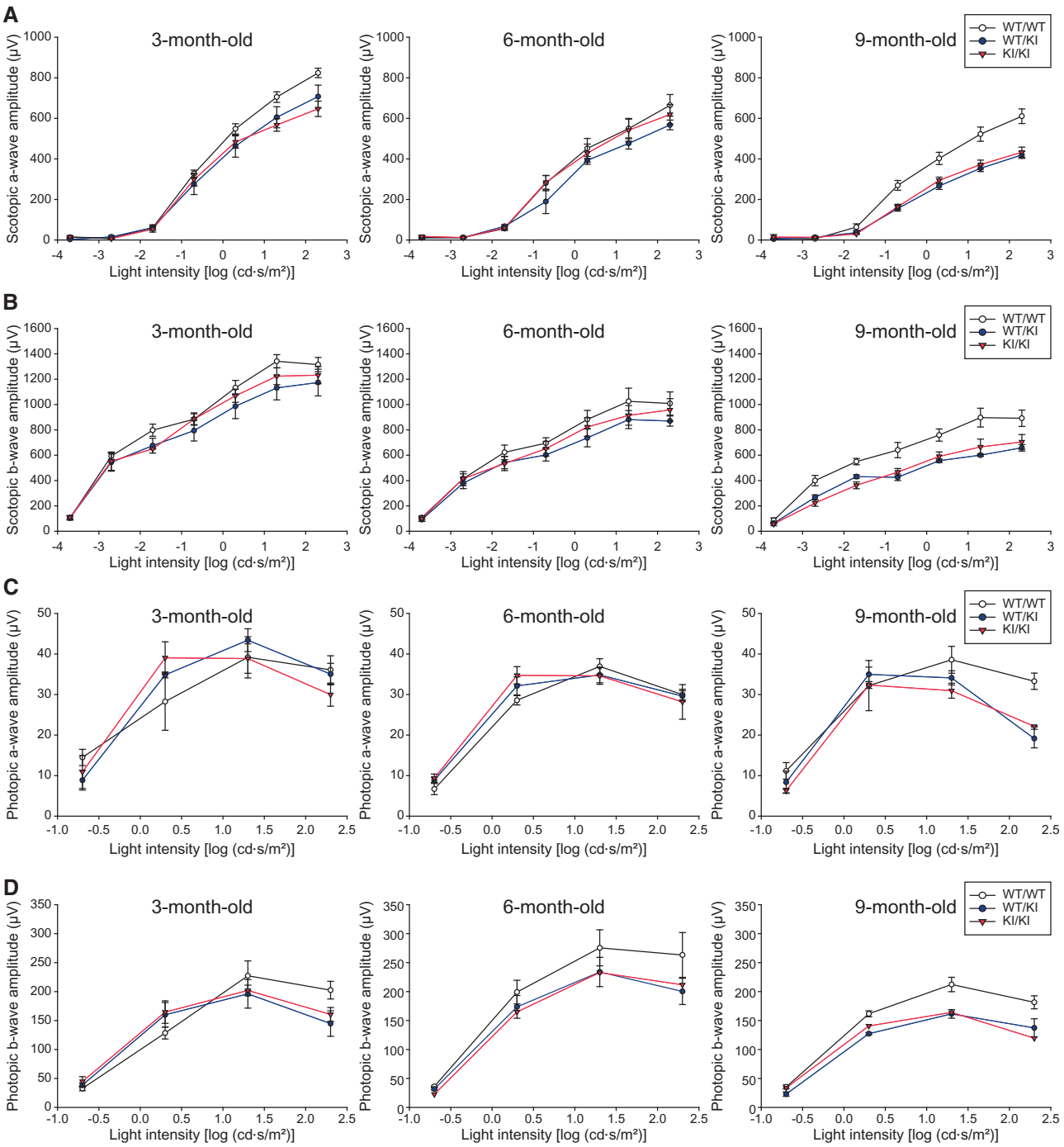

Figure 6. ERG responses of wild-type (WT/WT), heterozygous (WT/KI) and homozygous (KI/KI) mice at 3, 6 and 9 months of age. (**A**) To compare the retinal function between WT and KI mice, the scotopic a- and b-wave amplitudes were plotted as a function of light stimulus intensity (−3.7 to 2.3 log cd·s·m^2). The a-wave amplitude, which reflects the initial response of photoreceptors to a light stimulus, did not show significant difference between 3-month-old and 6-month-old WT/WT, WT/KI and KI/KI mice. However, at 9 months of age, both WT/KI and KI/KI mice displayed significant reduction in a-wave amplitudes compared with WT/WT mice ($P < 0.01$), suggesting that the mutation may cause a delayed onset of pathological phenotype. (**B**) Likewise, the amplitudes of the scotopic b-wave, which reflects the response of downstream retinal neurons to photoreceptor stimulation, also began to decline in 9-month-old WT/KI and KI/KI mice compared with WT/WT mice ($P < 0.05$). (**C**) To specifically examine the cone function, the photopic a- and b-wave amplitudes were plotted as a function of light stimulus intensity (−0.7 to 2.3 log cd·s·m^2). Similar to the results of scotopic ERG, the photopic a-wave amplitude began to decline in 9-month-old WT/KI and KI/KI mice ($P < 0.05$). (**D**) The photopic b-wave amplitude was also reduced in 9-month-old WT/KI and KI/KI mice ($P < 0.05$). Different sets of animals were used for ERG recordings at each time point. $n = 4$ for the WT/WT group, $n = 4$ for the WT/KI group, $n = 4$ for the KI/KI group. Data are shown as mean ± S.E.M.

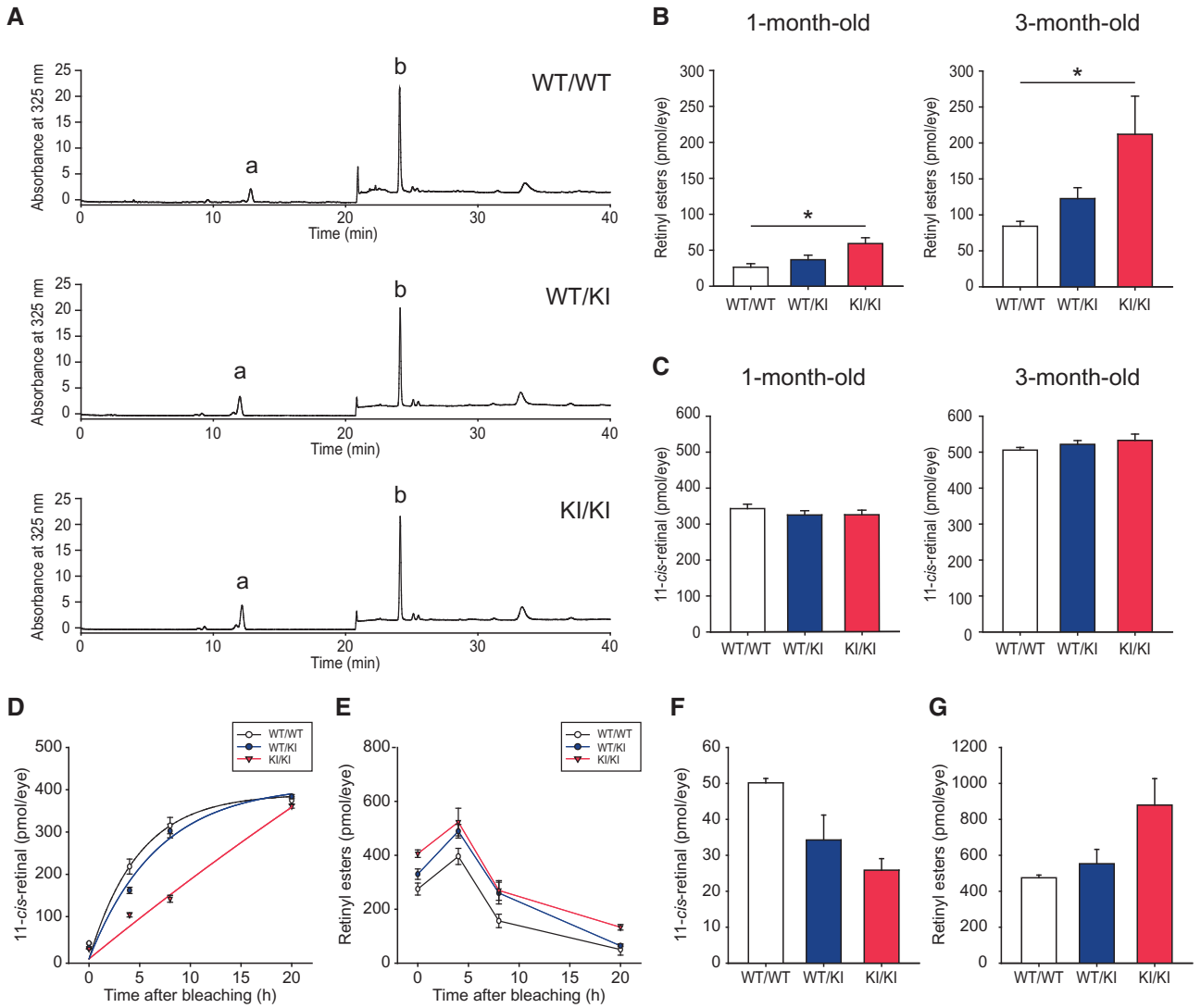

Figure 7. Retinoid profile of D477G KI mice and analysis of 11-*cis*-retinal regeneration after bleaching. (**A**) HPLC chromatograms showing the retinoid composition of eye extracts from fully dark-adapted wild-type (WT/WT), heterozygous (WT/KI) and homozygous (KI/KI) mice. Peaks in the chromatograms were identified based on elution time and characteristic UV/vis absorbance spectra. Peaks 'a' correspond to retinyl esters and peaks 'b' correspond to 11-*cis*-retinal. (**B**) Amount of retinyl esters in fully dark-adapted wild-type, heterozygous and homozygous mice. $n = 6$ for 1-month-old WT/WT group, $n = 8$ for 1-month-old WT/KI group, $n = 4$ for 1-month-old KI/KI group, $n = 4$ for 3-month-old WT/WT group, $n = 4$ for 3-month-old WT/KI group and $n = 3$ for 3-month-old KI/KI group. * indicates $P < 0.05$. Data are shown as mean ± S.E.M. (**C**) Amount of 11-*cis*-retinal in fully dark-adapted wild-type, heterozygous and homozygous mice. $n = 6$ for 1-month-old WT/WT group, $n = 8$ for 1-month-old WT/KI group, $n = 4$ for 1-month-old KI/KI group, $n = 4$ for 3-month-old WT/WT group, $n = 4$ for 3-month-old WT/KI group and $n = 3$ for 3-month-old KI/KI group. Data are shown as mean ± S.E.M. Differences between groups all had *P*-values > 0.05. (**D**) Regeneration of 11-*cis*-retinal following a bleach (5000 lux light for 10 min) in 3-month-old wild-type, heterozygous and homozygous mice after 0, 4, 8 and 20 h of dark adaptation. $n = 3$–4 for each time point. The recovery of the chromophore was significantly delayed in heterozygous mice until 4 h of dark adaptation ($P < 0.05$) and homozygous mice until 8 h of dark adaptation ($P < 0.001$). Data are shown as mean ± S.E.M. Significance between groups was determined with one-way ANOVA and the Bonferroni post-test. Curve fitting was performed with the following equation in SigmaPlot [exponential rise to the max; $y = a(1 - e^{-bx})$]. (**E**) Changes of retinyl esters following a bleach (5000 lux light for 10 min) in 3-month-old wild-type, heterozygous and homozygous mice after 0, 4, 8 and 20 h of dark adaptation. $n = 3$–4 for each time point. Data are shown as mean ± S.E.M. (**F**) Regeneration of 11-*cis*-retinal following a bleach (5000 lux light for 10 min) in 9-month-old wild-type, heterozygous and homozygous mice after 10 min of dark adaptation. $n = 3$ for the WT/WT group, $n = 5$ for the WT/KI group and $n = 3$ for the KI/KI group. Data are shown as mean ± S.E.M. (**G**) Levels of retinyl esters following a bleach (5000 lux light for 10 min) in 9-month-old wild-type, heterozygous and homozygous mice after 10 min of dark adaptation. $n = 3$ for the WT/WT group, $n = 5$ for the WT/KI group and $n = 3$ for the KI/KI group. Data are shown as mean ± S.E.M.

presented on RPE65 D477G expression and activity in mammalian cells (Fig. 1A and E).

Crystallization and structural determination of the ACO/RPE65 D477 chimera

To directly examine the structural preservation of the D477 loop in RPE65 and the ACO/RPE65 chimera, we crystallized ACO/RPE65–477 loop under the same conditions used for WT ACO (36). The crystals diffracted X-rays to ~2.5 Å resolution and were isomorphous to the previously reported orthorhombic crystal form of ACO with four monomers in the asymmetric unit (Table 2) (37). Inspection of the initial electron density maps revealed clear difference density for the substituted residues. Following refinement (Table 2), we found the loop conformation to be nearly identical to that of RPE65 with an overall root-mean-square

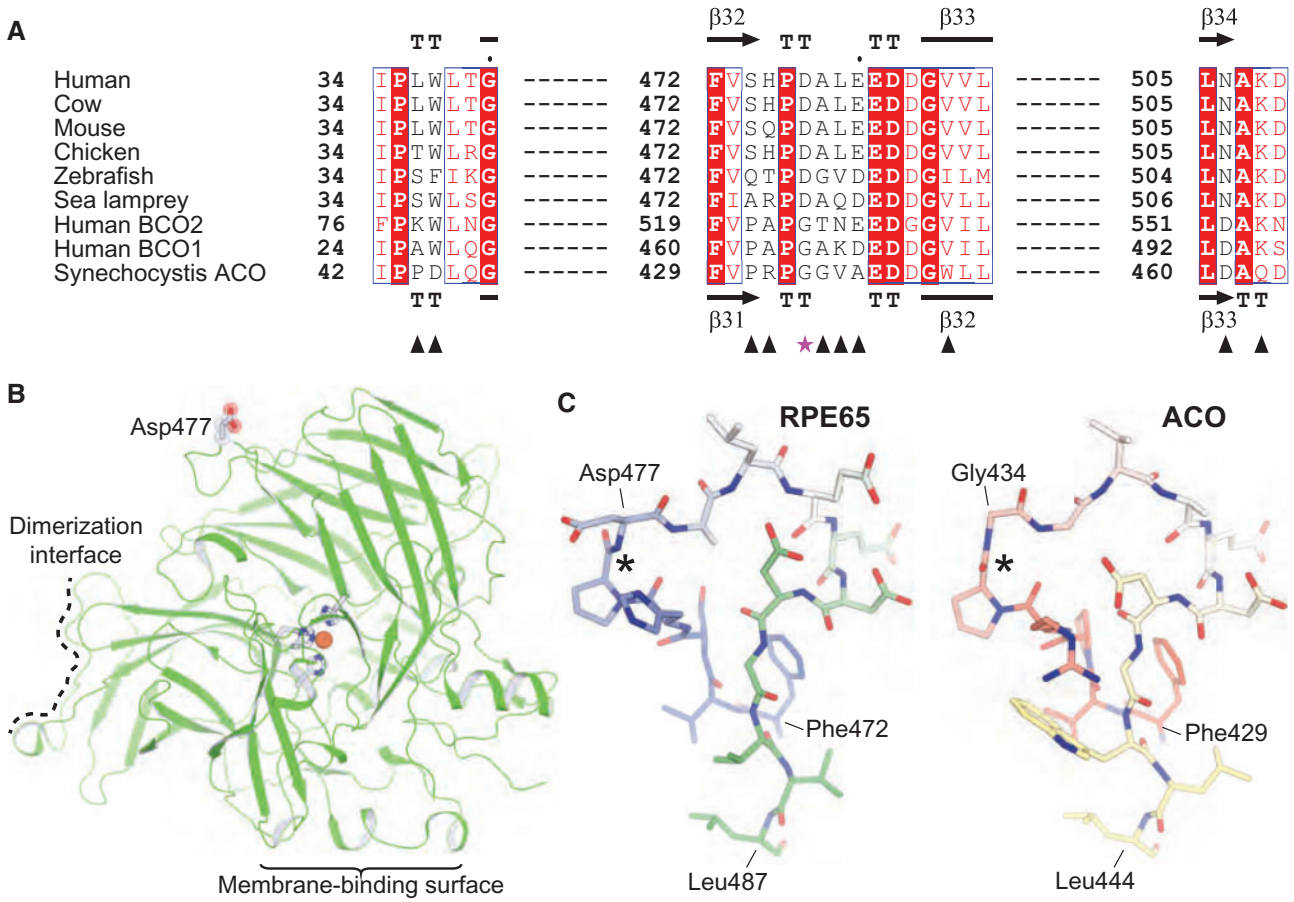

Figure 8. Structural analysis of the D477 loop region in RPE65 and its homologs. (**A**) Alignment of RPE65 orthologs, human BCO enzymes and *Synechocystis* ACO amino acid sequences. Positions swapped to generate the ACO/RPE65 chimera are marked with black triangles. The purple star marks position 477 in RPE65. Numbers in front of the aligned sequences denote the beginning sequence position. Secondary structure elements determined by X-ray crystallography for RPE65 and ACO are displayed on the top and bottom of the aligned sequences, respectively. (**B**) Location of the Asp477 loop within the three-dimensional structure of RPE65. (**C**) *left*—Stick representation of the RPE65 loop region containing Asp477. *Right*—Stick representation of the corresponding loop in ACO. Note the close structural similarity between the two proteins as well as the difference in β-turn conformation marked by an asterisk.

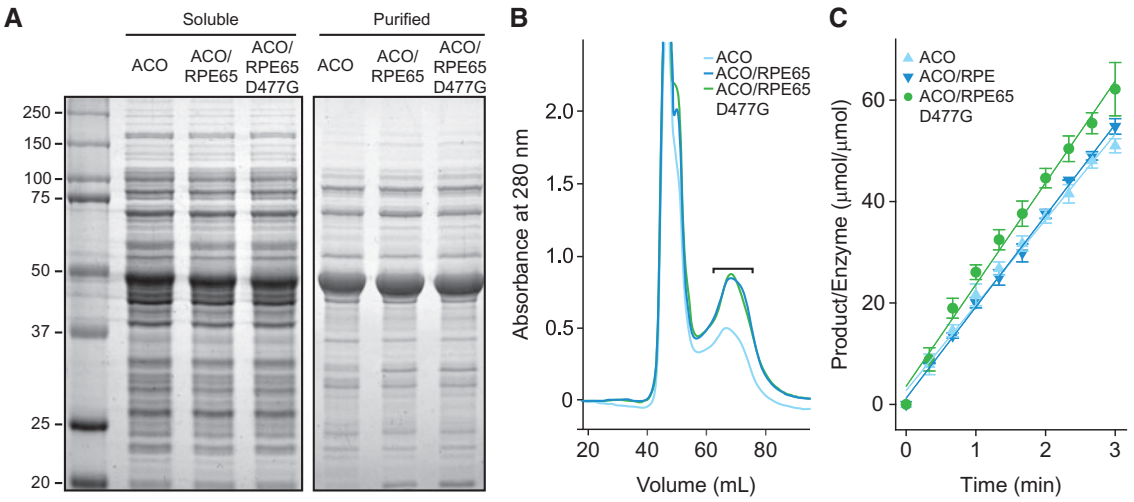

Figure 9. Expression, purification and enzymatic activity of ACO/RPE65 chimeras. (**A**) SDS-PAGE of soluble fractions obtained from lysates of *E. coli* expressing the indicated constructs (left) as well as the corresponding final purified protein samples (right). Proteins were visualized by Coomassie Blue staining. (**B**) Gel filtration elution profiles of the indicated proteins. The horizontal bracket indicates the protein peak corresponding to monomeric protein. (**C**) Apocarotenoid oxygenase activity of the three purified proteins. Data are shown as mean ± SD from three separate experiments each performed in triplicate.

Table 2. X-ray diffraction data collection and structure refinement statistics

Data collection and processing			
Crystal	ACO/RPE65 chimera	ACO/RPE65 chimera D477G[a] trigonal crystal form	ACO/RPE65 chimera D477G monoclinic crystal form
X-ray source	NSLS-II 17-ID-2	APS 24-IDE/NSLS-II 17-ID-1	NSLS-II 17-ID-1
Wavelength (Å)	0.979357	0.97918/0.918401	0.918401
Space group	$P2_12_12_1$	*P*312	*C*2
Unit cell lengths (Å)	$a = 119.35$, $b = 125.66$, $c = 204.41$	$a = 126.52$, $c = 159.767$	$a = 191.43$, $b = 56.17$, c = 136.91
Unit cell angles (°)			$\beta = 133.83$
Resolution (Å)[b]	50—2.5 (2.65 – 2.5)	50—3.15 (3.23—3.15)	50—2.60 (2.76—2.60)
Unique reflections	106654 (16940)	25537 (4090)	31744 (5023)
Multiplicity	8.7 (8.6)	18.6 (18.0)	3.1 (3.0)
Completeness (%)	99.8 (99.4)	99.9 (100)	96.7 (96)
$<I/\sigma I>$	9.5 (0.99)	16.0 (1.2)	11.6 (0.93)
$R_{merge}I$ (%)	19.6 (175.2)	12.5 (291.6)	6.6 (99.8)
$CC_{1/2}$ (%)	99.6 (52.5)	100 (67.3)	99.8 (48.9)
Wilson *B* factor (Å^2)	62	121	76
Refinement			
Resolution (Å)	48.84–2.5	49.65–3.15	41.76 (2.6)
No reflections[c]	101 462 (5100)	24 267 (1269)	30 156 (1588)
R_{work}/R_{free} (%)	18.1/21.7	23.2/26.6	22.0/26.0
No atoms	15 813	7541	7546
Protein	15 082	7536	7491
Iron	4	2	2
Water	725	3	53
<B-factor> (Å^2)	62	168	79
Protein	62	168	79
Iron	53	177	80
Water	56	106	58
RMS deviations			
Bond lengths (Å)	0.012	0.006	0.007
Bond angles (°)	1.53	0.968	1.11
Ramachandran plot (% favored/outliers)[4]	97.9/0	95.3/0	96.9/0
Molprobity score (%)	100	100	100
PDB accession code	6C7K	6C7O	6C7P

[a]Data from two isomorphous crystals were merged to produce the final dataset.
[b]Values in parentheses are for the highest resolution shell of data.
[c]Values in parentheses are the number of reflections used for cross-validation.

difference (RMSD) of 0.56 Å for all atoms in the loop based on a global superposition of the two structures (Fig. 10A). These results validated our use of ACO/RPE65-D477 loop to infer the structural consequences of the RPE65 D477G mutation.

Crystallization and structural determination of the ACO/RPE65 D477G mutant

Next, we crystallized the D477G chimera variant again under the same conditions used for WT ACO. Strikingly, this single amino acid change resulted in the formation of trigonal and monoclinic crystals unprecedented amongst prior ACO and RPE65 crystallographic studies. These crystals grew either alone or as polymorphs with both forms present in a single drop (Supplementary Material, Fig. S4), whereas the original orthorhombic crystals were not observed for the point mutant. The trigonal crystals diffracted X-rays anisotropically to ~3.1 Å resolution and belonged to the rare space group *P*312 with two molecules in the asymmetric unit. The monoclinic crystals diffracted X-rays more isotropically to a resolution of ~2.6 Å and belonged to space group *C*2, also with two molecules in the asymmetric unit (Table 2). Refined structures of these two crystal forms revealed the expected absence of an aspartic acid side chain at position 434 (equivalent to position 477 in RPE65). The overall structure of the D477G loop region was like that of the D477 chimera (main chain RMSD of 0.48–0.86 Å depending on the specific chain) with a few notable differences (Fig. 10B and C). Focusing on the monoclinic crystal form for which the electron density support was strongest, the D477G-containing β−turn was found in both a type-I (chain A) and a type-II (chain B) conformation. This variability is not unexpected given the conflicting tendencies of the His residue in position "n" to favor a type-I conformation through hydrogen bonding with the amide nitrogen of residue 434 and the glycyl residue at the n + 2 position allowing the flipped orientation of the 433–434 peptide bond characteristic of a type-II turn. Additionally, Leu436 was displaced by ~0.5–1.4 Å, depending on the subunit, and the side chains for Glu437 and Glu440 adopted different rotameric conformations compared with the ACO/RPE65-D477 loop. The latter alterations are likely due to a difference in crystal packing as discussed below. In both crystal forms, the electron density

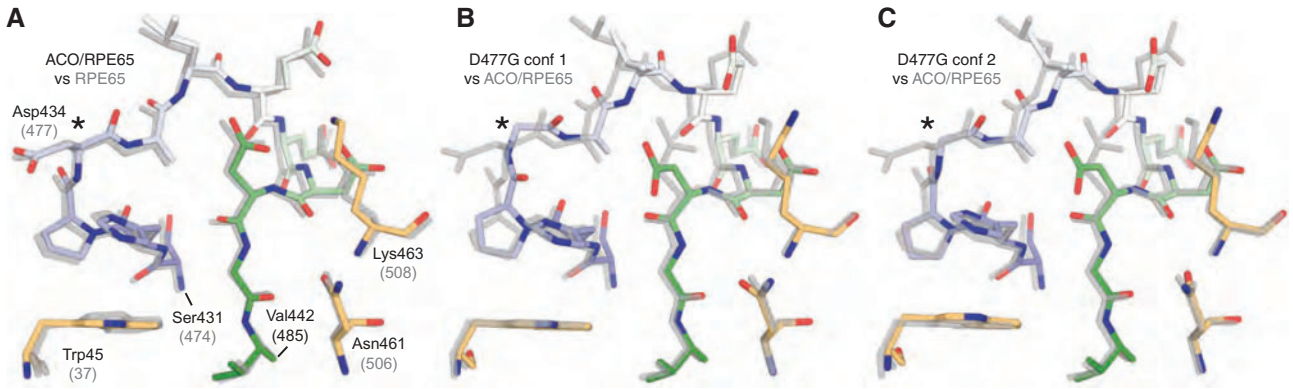

Figure 10. Structure of the D477 loop region in ACO/RPE65 chimera proteins. (**A**) Structure of the D477 loop region in ACO/RPE65 chimera (blue to green gradient) compared with bovine RPE65 (gray). Auxiliary substituted residues in ACO/RPE65 chimera and the corresponding residues in bovine RPE65 are colored light orange and gray, respectively. The Leu residue substituted at position 44 is omitted for clarity. The D477 position is marked by an asterisk. Top residue labeling refers to the ACO/RPE65 sequence whereas the numbers on bottom (in gray) refer to the native RPE65 sequence. Note the close structural correspondence between the two proteins in this region. (**B**) Comparison of the same loop region of ACO/RPE65 D477G chimera monoclinic crystal form with the ACO/RPE65 D477 chimera (shown in gray). (**C**) Same as panel B but showing the conformation of the second molecule located in the asymmetric unit of the monoclinic crystal form. Note the two distinct orientations of the β-turn marked with asterisks with (**B**) showing a type II turn and (**C**) showing a type I turn.

corresponding to the D477 loop and surrounding residues was well resolved indicating that the D477G substitution does not structurally destabilize this loop region.

The D477G substitution causes a gain of protein–protein interaction potential for the 477 loop

Molecular packing in the D477G crystals differed in a striking way from that of the original ACO/RPE65-D477-loop protein. Whereas the D477 loop was not involved in significant protein–protein contacts in the former crystal form (Supplementary Material, Fig. S5), contacts involving this loop were integrally involved in the crystal packing of both new crystal forms (Fig. 11). In the trigonal crystals, the D477G loop regions of the two monomers within the asymmetric unit engage in two non-equivalent protein–protein interactions with contact surface areas of 477 and 411 Å^2 involving predominantly van der Waals interactions with a few H-bonds and salt bridges (Fig. 11A and B). The two interactions occur at roughly the same site of the ACO/RPE65-D477G molecule but are rotated by 180° with respect to each other and involve two distinct sets of residues. In the monoclinic crystals, the D477G loop regions of the two molecules in the asymmetric unit engage in two non-identical but similar protein–protein interactions with contact surface areas of 415 and 389 Å^2 (Fig. 11C and D). The two contact points are related by a slight rotation and involve similar sets of residues forming distinct combinations of van der Waals and polar/ionic interactions. In both crystal forms, these predominantly hydrophobic interactions involving the D477G loop are among the major contact points responsible for crystal formation. In all four cases, multiple van der Waals interactions formed between the G434 α carbon and interacting residues indicate that the absence of the Asp side chain at position 434 crucially enabled formation of the protein–protein contacts. The D477G substitution thus triggered a gain of protein–protein interaction potential by allowing the 477 loop to form contacts with diverse molecular surfaces.

Discussion

Until recently, RPE65-associated RP and LCA were only known to occur as recessive diseases with complete penetrance and generally early onset, typically progressing to legal blindness within the first or second decade of human life (38). The discovery of a phenotypically distinct, dominant form of RPE65-associated RP linked to the D477G mutation with a different time course of disease and incomplete penetrance was thus surprising when it was reported (9). The D477G mutation is qualitatively different from other pathogenic RPE65 mutations reported to date. Recessive RP-associated mutations are typically located in critical active site regions or at the interfaces of the beta propeller blades, which directly affect the catalytic activity, folding trajectory or tertiary structure stability of the enzyme (13). By contrast, D477 is located in a solvent-exposed loop located away from functionally critical regions of the protein (Fig. 8B). It is also striking that closely related RPE65 family members encode a Gly residue at a position in their protein chain equivalent to residue 477 in RPE65 (Fig. 8A). Hence, the pathogenic mechanism of this missense mutation has remained mysterious, although it was previously proposed that the D477G substitution could result in protein misfolding and/or aggregation (9,10).

In this report, we provide evidence that the D477G substitution does not induce a protein-folding defect, similarly sparing any significant perturbation of the three-dimensional structure and catalytic activity of the protein. Instead, we find that it changes the physiochemical properties of the D477-containing loop to produce an aggregation-prone surface capable of engaging in abnormal protein–protein interactions. This change in interaction potential was directly observed at high resolution with an ACO/RPE65 chimeric protein containing the D477 loop and surrounding residues of RPE65. The change of position 477 from Asp to Gly in this protein with all other experimental variables held constant enabled the 477 loop to engage in diverse protein–protein interactions, as observed by crystal packing analysis in two distinct crystal

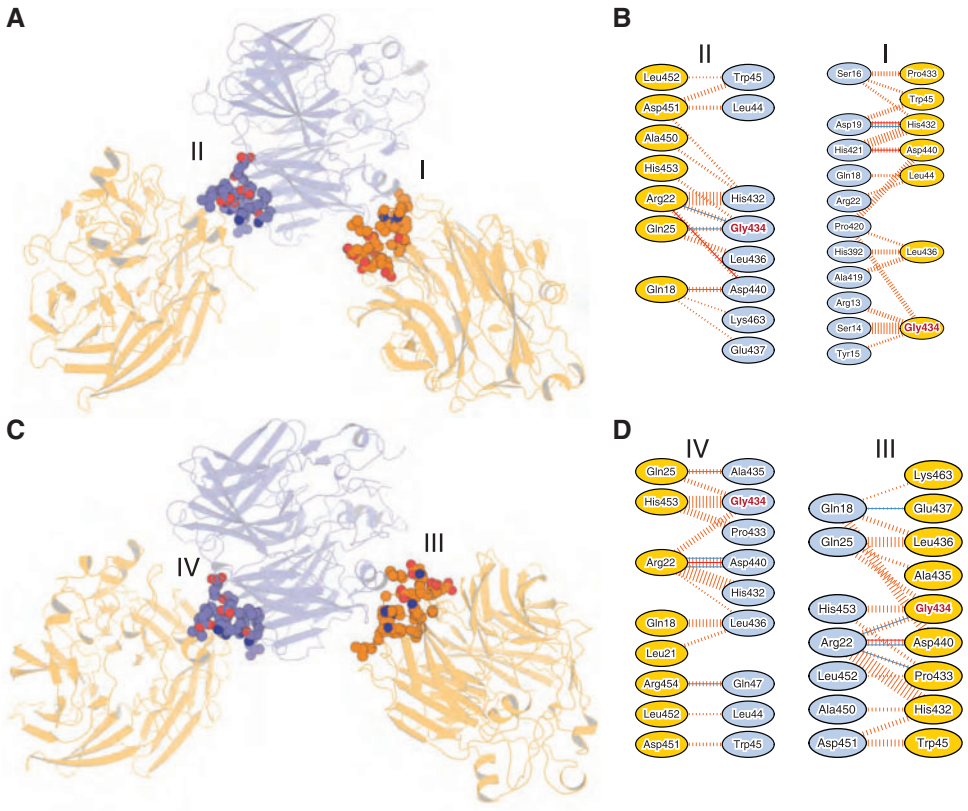

Figure 11. Involvement of the D477 loop in crystal packing of ACO/RPE65 chimera D477G mutant. (**A**) Molecular packing observed in the trigonal crystal form revealing an interaction of the D477G loop and surrounding residues (all shown as van der Waals spheres) with the second molecule in the asymmetric unit (contact I). This second molecule in turn also interacts with a symmetry-related molecule through the region surrounding the D477G loop (contact II). (**B**) Details of the interactions formed between the D477G loop and surrounding residues with the interaction partner. Dashed lines indicate van der Waals contacts (width proportional to number of atomic contacts), solid blue lines indicate hydrogen bonds and solid red lines indicate salt bridges. (**C**) Molecular packing of molecules in the monoclinic crystal form mediated by the D477G loop and surrounding residues. Contact III involves the two molecules in the asymmetric unit whereas contact IV involves a symmetry-related molecule. These two contacts are related by a slight rotation. (**D**) Interactions formed between the D477G loop and residues from interacting partners in the monoclinic crystal form. In all four unique contacts, the introduction of an Asp side chain at position 434 would result in steric clashes which explains why these two crystal forms are only observed for the D477G mutant.

forms. Among the possible interactions that could be altered *in vivo*, we observed that D477G RPE65 is subject to recognition by ubiquitin ligases, likely due to the increased hydrophobicity of the 477 loop imparted by loss of the negatively charged Asp side chain (Supplementary Material, Fig. S6). This interpretation is supported by previous studies demonstrating that hydrophobic surfaces with the potential to cause insolubility or aggregation are recognized by the Ubc6/Ubc7-containing ubiquitination complex (39). Ubiquitination of RPE65 likely targets it for proteasomal degradation as reported previously for recessive RP-associated RPE65 mutations *in vitro* (17). A similar phenomenon was also observed in R91W RPE65 KI mice, where mutant RPE65 was polyubiquitinated and subsequently degraded by the 26S proteasome (19). We observed that the degree of ubiquitination and degeneration was more extensive in homozygous KI mice, consistent with the retinoid profile in such mice. Therefore, two copies of the mutant allele in homozygous KI mice exacerbated their phenotypes, which could be interpreted as the D477G allele being semi-dominant (40). Besides the protein-associated effect, we also observed that the c.1430G>A point mutation reduces mRNA levels relative to WT RPE65 mRNA, suggesting a defect in RNA stability or processing (Fig. 12). It remains possible that the reduction in D477G mRNA is a result of the remaining loxP site in the mutant allele. Nevertheless, total RPE65 mRNA levels were comparable between the three genotypes as observed previously (11) suggesting that reduced processing or stability of D477G mRNA can be compensated for by transcriptional upregulation.

The reduced levels of RPE65 we and others have observed in D477G KI mice raise the possibility of haploinsufficiency being involved in the disease pathogenesis. Although a few studies have suggested the possibility of retinal disease in carriers of recessive RP-associated RPE65 alleles (16,41), others specifically looking at the potential presence of retinal disease in RPE65-null mutant carriers have consistently concluded that heterozygous loss of RPE65 function (pure haploinsufficiency) does not adversely affect visual function or retinal structure in a clinically meaningful way (42–44). Likewise, P25L and R91W KI mice, which are models of mild and severe RP, respectively, do not exhibit abnormal visual phenotypes in marked contrast to the respective homozygous KI mice. Heterozygous RPE65 KO mouse retinal structure and function are also indistinguishable from WT mice (4). Thus, haploinsufficiency appears not to underlie the retinal structural and functional defects associated with the D477G mutation.

The potential pathogenic mechanisms mentioned in the preceding text help explain the phenotypes we and others (11) have observed in RPE65 D477G KI mice. These mice exhibit an

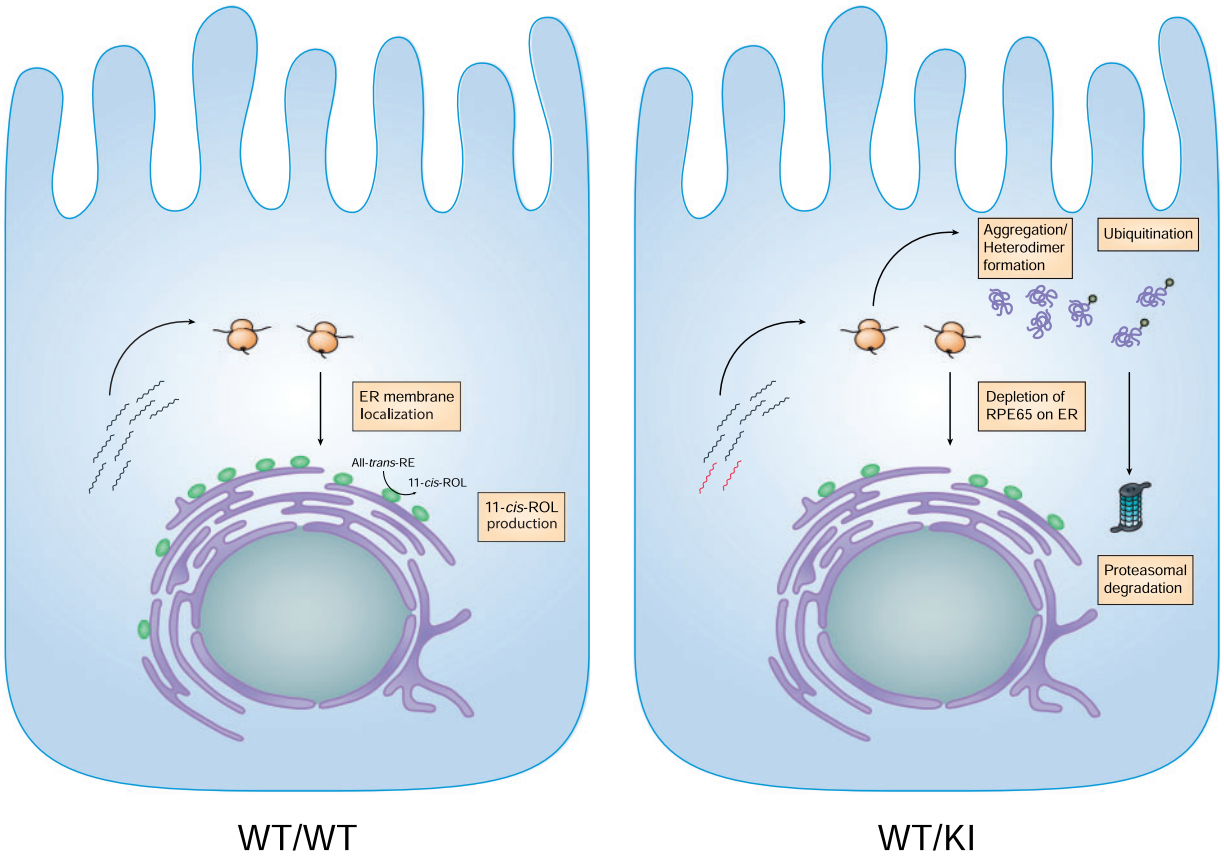

Figure 12. Schematic diagram showing a proposed pathogenic mechanism of RP resulting from the D477G RPE65 mutation. In the RPE of WT/WT mice, RPE65 is localized in the ER membrane following translation and contributes to the visual cycle by isomerizing all-*trans*-retinyl esters to form 11-*cis*-retinol. In RPE of WT/KI mice, mRNA from the D477G *RPE65* allele is significantly reduced. The hydrophobic neomorphic surface of D477G RPE65 could produce aggregates in the cytoplasm and impair the ER localization of RPE65. Due to the possibility of dimerization between D477G and WT RPE65, the mutation could also result in mislocalization of WT RPE65 resulting in a dominant-negative effect as described previously for D477G KI mice. The aggregates are ubiquitinated and degraded by proteasomes.

overall visual cycle insufficiency manifested by ERG suppression in older mice, a delay in visual chromophore regeneration and the accumulation of retinyl esters in both heterozygous and homozygous mice. These phenotypes can be attributed to reduced levels of functional RPE65 in KI mice, likely due to a reduction in RPE65 protein levels resulting from its ubiquination and proteolytic degradation (Fig. 12) as well as a potential dominant-negative effect exerted by the D477G mutant on visual chromophore production which could suppress visual cycle activity to a pathogenic level (11). Given that RPE65 is likely a dimeric protein *in vivo* (32), the dominant-negative effect could be explained by heterodimer formation between WT and D477G resulting in potential mislocalization and/or degradation of the dimeric complex, thus reducing WT protein function (Fig. 12).

Besides effects on visual cycle function, we also observed pathological autofluorescent bodies in the retinas of heterozygous and homozygous KI mice by SLO imaging. Although these structures cannot be definitively identified by SLO, prior studies on animal disease models including *Palm*$^{-/-}$ (20), E150K opsin (22) and *ABCA4*$^{-/-}$/*Rdh8*$^{-/-}$ (23) mice indicate that autofluorescent bodies reflect the infiltration of phagocytic cells into the retina. In addition to this abnormality, we also observed a mild decrement in photoreceptor number in mice of both genotypes relative to WT controls by OCT imaging. This loss of photoreceptors could originate either from visual chromophore deficiency as described previously for RPE65-associated recessive RP or from a generalized RPE dysfunction that perturbs the ability of the RPE to support photoreceptor health (45). The latter mechanism, which implicates a direct toxic effect of D477G RPE65 on the RPE, is suggested by RPE hypertrophy and choroidal atrophy observed in humans carrying the RPE65 D477G substitution (9,10). We note that the mild loss of photoreceptors in these KI mice cannot fully account for the observed decrease in ERG responses, which again points to visual cycle insufficiency in these animals.

Although gain-of-function mutations affecting protein folding and aggregation are most frequently associated with the formation of intracellular fibrils and amyloid as in Alzheimer disease and systemic amyloidosis (46), such mutations can also exert subtler effects on cellular homeostasis not involving formation of beta-amyloid or other beta-sheet rich aggregates (47,48). Recent studies on protein–chaperone interactions have suggested that potentially aggregation-prone regions of a protein are frequently protected by so-called “gatekeeper” residues present within the peptide sequence (48,49). These typically hydrophilic residues (Arg, Lys, Glu and Asp) interrupt regions of hydrophobicity and may also increase surface entropy at otherwise aggregation-prone sites of a protein. Our data suggest that D477 could serve such a role in RPE65, as the Gly replacement allows formation of predominantly hydrophobic contacts that would be prohibited by the negatively charged Asp side chain.

Loss of a surface-exposed gatekeeper residue leading to the aggregation of properly folded protein molecules, as we suggest here for D477G RPE65, has previously been documented for the sickle-cell anemia-associated E6V substitution in hemoglobin (known as hemoglobin S), which predisposes the protein to abnormal oligomerization (50). This mutation does not affect the secondary, tertiary or quaternary structures of hemoglobin at normal oxygen concentrations (51). However, during hypoxia, the protein can form abnormal homo-oligomers that generate characteristic sickling of red blood cells. Individuals carrying one abnormal allele only exhibit symptoms of sickle-cell anemia in the presence of stressors such as severe hydration or high-intensity physical activity (52–54). Considering the relatively mild phenotype in the D477G KI mouse model and the incomplete penetrance of D477G-associated disease in humans (9,10), the pathogenic mechanism of D477G conceivably requires extra factors such as environmental stressors and age-related physiological changes as triggers.

The R36S mutation in γD crystallin also exhibits abnormal protein–protein interactions enabled by loss of a gatekeeper residue that leads to dominant ophthalmic disease in spite of preserved native tertiary structure of the mutant protein (55). The R36S missense mutation results in the formation of a novel protein–protein interaction surface that allows crystallin to crystallize in the lens. Notably, the structure of the mutant protein was determined from an actual crystal extracted from the affected patient's lens, which showed that the site of mutation allowed formation of new, predominantly hydrophobic protein–protein interactions (55). Other crystallin mutants have also been shown to exhibit abnormal aggregation behavior but with preserved tertiary structures (56). While we do not present data that suggests the D477G promotes abnormal RPE65 homo-oligomerization, the same concept of abnormal hydrophobic interactions could be applicable to RPE65 heterotypic interactions within the cell. Indeed, the fact that RPE65 is relatively abundant within the RPE suggests that it could be present at sufficient levels to generate substantial cellular stress through binding to cellular components.

The D477G RPE65 KI mouse that we report here recapitulates some but not all features of the human disease. As mentioned above, additional stressors required for the full phenotypic expression of the disease that are experienced by humans but not mice in a well-controlled laboratory environment could underlie the differences in disease severity. Lack of a macula in mouse retina might be another key factor contributing to the phenotypic discrepancy between humans and mice. Several patients with the D477G mutation developed a dystrophy of the macula, which is the area of highest cone density (9,10). In addition, mouse RPE conceivably could tolerate the existence of mutant RPE65 and clear protein aggregation products more effectively than human RPE. Therefore, RPE cells or 3-D retinal organoids differentiated from human-induced pluripotent stem cells carrying the D477G RPE65 mutation could be alternative tools for future studies on the pathogenesis and treatment of this form of RP.

Materials and Methods

Animals

D477G KI mice were generated by the InGenious Targeting Laboratory (Ronkonkoma, NY). C57BL/6J WT mice (Jackson Laboratory, Bar Harbor, ME) were used for mating with D477G KI mice. Mice were housed at the animal resource center at Case Western Reserve University School of Medicine in a 12-h light (<10 lux)/12-h dark cyclic environment with *ad libitum* access to food (LabDiet 5053) and water. All animal procedures and experiments were approved by the Institutional Animal Care and Use Committee of Case Western Reserve University, conformed to the recommendations of the American Veterinary Medical Association Panel on Euthanasia and were conducted in accordance with the Association for Research in Vision and Ophthalmology Statement for the Use of Animals in Ophthalmic and Visual Research.

Generation of D477G KI mice

D477G KI mice were generated as follows: a 11.3 kb region used to construct the targeting vector was first subcloned from a positively identified C57BL/6 BAC clone. The construct was designed as follows: the 5′ homology arm extended 8.9 kb 5′ to the KI mutation; the 3′ homology arm extended 2.2 kb 3′ to the FRT flanked Neo cassette; the Neo cassette was inserted between exons 13 and 14; exon 13 with a point mutation was engineered by three-step PCR mutagenesis to introduce A>G mutations resulting in Asp to Gly substitutions. This BAC construct was subcloned into a 2.45 kb backbone vector (pSP72, Promega, Madison, WI) containing an ampicillin selection cassette for transformation of the construct before electroporation. The targeting vector was linearized by NotI and then electroporated into embryonic stem cells (129/SvEV X C57BL/6 FLP hybrid) expressing FLP recombinase. After selection with G418 antibiotic, positive clones were expanded for PCR analysis (FN1 forward, 5′-TATCCGTACGTTCGTGGGATTGTC-3′; and A3 reverse, 5′-AGAACTTCTCGAGGACTCACCAGG-3′) and southern blotting analysis to identify recombinant ES clones. Validated clones were then microinjected into C57BL/6 blastocysts, and the resulting chimeric mice with a high percentage of agouti coat color were mated with C57BL/6 mice (InGenious Targeting Laboratory) to generate germline Neo-deleted mice. These founders were then screened for deletion of the Neo Cassette by PCR analysis (SC1 forward, 5′-GCATACGGACTTGGGTTGAAT CAC-3′; and NDEL2 reverse, 5′-ACTATGCTGCAGAAGGTGTTT TACTGTGG-3′) of their genomic DNA obtained from tail biopsies. The *Rd8* mutation in *Crb1* was absent in the animals used for this study (57).

Mutagenesis and stable transduction of NIH3T3 cell lines

An NIH3T3 cell line stably expressing LRAT was generated by a previously published protocol (58). The retroviral expression vectors were generated by introducing *Eco*RI and *Not*I restriction sites at the ends of the hRPE65 coding sequence by PCR with the following primers: forward, 5′-TAGGAATTCATGTCTATCCA GGTTGAG-3′; reverse, 5′-TAAGCGGCCGCTCAAGATTTTTTGAAC AG-3′. The modified hRPE65 cDNA was inserted into a pMX-IG retroviral vector provided by Dr. T. Kitamura from the University of Tokyo (59). An internal ribosomal entry site (IRES) and enhanced green fluorescence protein (EGFP) were placed downstream of the hRPE65 coding region, allowing co-expression of hRPE65 and EGFP from the same mRNA. The hRPE65 (D477G) mutation was introduced by PCR amplification of the entire plasmid by using Phusion High Fidelity polymerase (New England Biolabs, Ipswich, MA).

NIH3T3-LRAT-hRPE65 and NIH3T3-LRAT-hRPE65 (D477G) stable cell lines were generated by transduction of NIH3T3-

LRAT cells with retrovirus collected from Phoenix-Eco cells transfected with the pMXs-IG containing hRPE65 or hRPE65 (D477G) according to a previously published protocol (58). Transduced cells were sorted by a FACSAria cell sorter (BD Biosciences, San Jose, CA) to selectively collect transduced cells and ensure comparable EGFP expression between NIH3T3-LRAT-hRPE65 and NIH3T3-LRAT-hRPE65 (D477G).

Cells were maintained in growth medium (GM) composed of Dulbecco's modified Eagle's medium (Gibco, Gaithersburg, MD), pH 7.2, with 4 mM L-glutamine, 4500 mg/l glucose and 110 mg/l sodium pyruvate supplemented with 10% (v/v) heat-inactivated fetal bovine serum, 100 units/ml penicillin and 100 units/ml streptomycin. After reaching confluence, cells were washed twice with PBS, trypsinized, passaged and then maintained at 37°C in 5% CO_2.

Immunoblotting of RPE65

Cultured cells were lysed with 200 μl of RIPA buffer (Cell Signaling Technology, Danvers, MA) with protease inhibitors (Sigma-Aldrich, St. Louis, MO) and sonicated for 5 s to shear the DNA. Enucleated eyes from WT, heterozygous KI and homozygous KI mice were dissected and lysed according to a previously published protocol (60). Protein concentrations were determined with a BCA Assay kit (Bio-Rad, Hercules, CA) following the manufacturer's instructions. Protein samples were mixed with NuPAGE LDS sample buffer and NuPAGE reducing agent and then separated using NuPAGE 4–12% Bis–Tris gels (Invitrogen, Carlsbad, CA) and transferred to polyvinylidene difluoride (PVDF) membranes. Membranes were blocked with 5% (w/v) non-fat milk or 5% (w/v) BSA and then incubated with either anti-RPE65 monoclonal antibody (1: 1000) (61), anti-β-actin antibody (1: 1000) (Cell Signaling Technology) or anti-GAPDH antibody (Abcam, Cambridge, UK) overnight at 4°C. After washing with PBS containing 0.1% (v/v) Tween 20, membranes were incubated with peroxidase-linked anti-mouse or anti-rabbit IgG (1: 10 000) (Jackson ImmunoResearch Laboratories, West Grove, PA) for 1 h at room temperature. Protein bands were visualized after exposure to SuperSignal West Pico Chemiluminescent substrate (ThermoFisher Scientific, Waltham, MA).

Immunoprecipitation

Immunoprecipitation was performed with anti-ubiquitin antibody (Abcam) coupled to magnetic, protein G Dynabeads (Invitrogen). Total RPE cell extracts isolated from WT, heterozygous KI or homozygous KI mice (two eyes per genotype), prepared in RIPA buffer, were incubated with anti-ubiquitin antibody conjugated magnetic beads (1.5 mg beads and 12 μg antibody per reaction) for 20 min at room temperature under constant, mild agitation. The supernatant was then removed and kept for further analysis, and the beads were washed three times in PBS containing 0.1% (v/v) Tween-20 by gentle pipetting and subsequent removal of wash buffer. Proteins pulled down by the beads were eluted by incubation for 20 min in a room temperature Thermomixer (Eppendorf, Hauppauge, NY) at 300 rpm in 20 μl Elution Buffer (NuPAGE LDS sample buffer and NuPAGE sample reducing agent, mixed per manufacturer's instructions). The lysate, flow through and eluate were separated on a NuPAGE 4–12% Bis–Tris gel (Invitrogen). Immunoblotting was performed as described in the preceding section.

Immunocytochemistry

Cells were fixed with 4% (w/v) paraformaldehyde (ThermoFisher Scientific) for 10 min and permeabilized with PBST (PBS containing 0.1% Triton X-100) for 10 min. Then cells were blocked in PBST containing 5% goat serum at room temperature. Cells were immunostained with anti-RPE65 monoclonal antibody (1: 1000) and anti-Calnexin polyclonal antibody (1: 200) (Abcam) followed by the corresponding Alexa Fluor 647 anti-mouse IgG (1: 1000) (ThermoFisher Scientific), Alexa Fluor 594 anti-rabbit IgG (1: 1000) (ThermoFisher Scientific) and DAPI. Samples then were mounted in ProLong Gold antifade reagent (Invitrogen) and imaged with a Leica TCS SP8 confocal microscope.

Retinoid isomerization activity assay

NIH3T3-LRAT-hRPE65 or NIH3T3-LRAT-hRPE65 (D477G) cells were plated in six-well culture plates at 0.8×10^6 cells per well in GM. The isomerization reaction was initiated 16 h later by replacing GM with fresh GM containing 10 μM all-*trans*-retinol delivered in *N, N*-dimethylformamide. Cells shielded from light were maintained at 37°C in 5% CO_2. After 16 h, cells and medium were collected, mixed with an equal volume of 4 M KOH in methanol and incubated at 52°C for 2.5 h to hydrolyze retinoid esters. Next, an equal volume of hexane was added, and the mixture was vigorously shaken. Following a 15 min centrifugation at 4000 rpm to facilitate phase separation, the organic phase was collected, dried *in vacuo* and dissolved in 250 μl of hexane. Extracted retinoids were separated on a normal phase HPLC column (Sil; 5 μm, 4.6×250 mm; Agilent Technologies, Santa Clara, CA) equilibrated with 10% ethyl acetate in hexane at an isocratic flow rate of 1.4 ml/min. 11-*cis*-retinol was detected by its characteristic retention time and absorption spectrum and quantified by correlating peak areas to a standard curve.

Real-time PCR analysis

Total RNA from the RPE layer of WT, heterozygous KI and homozygous KI mice was isolated according to a previously published method (62). cDNA was synthesized with a high capacity RNA-to-cDNA kit (Applied Biosystems, Foster City, CA) following the manufacturer's instructions. The same amount of total RNA was processed without reverse transcriptase as a negative control. Real-time PCR was performed using iQ™ SYBR Green Supermix (Bio-rad) with the following primers: forward, 5′-TATGAAGAC AATGGATTTCTGATTGTGGATCTCTGTTGCT-3′'; reverse, 5′-ATG TTCAGGATCTTTTGAACAGTCCATGGAAGGTCACAGG-3′. *Gapdh* was used as a housekeeping gene for normalization. Triplicate real-time PCR reactions were performed for each animal.

RPE65 cDNA fragment cloning

Total RNA from the RPE layer of WT, heterozygous KI and homozygous KI mice was isolated according to a previously published method (62). cDNA was synthesized with a high capacity RNA-to-cDNA kit (Applied Biosystems, Foster City, CA) following the manufacturer's instructions. The same amount of total RNA was processed without reverse transcriptase as a negative control. PCR was performed using Phusion High-Fidelity PCR Master Mix with the following primers: forward, 5′-TATGAAGACAATGGATTTCTGATTGTGGATCTCTGTTGCT-3′;

reverse, 5′-ATGTTCAGGATCTTTTGAACAGTCCATGGAAGGTCA CAGG-3′. The 655-bp predicted PCR products were not generated by negative controls involving either non-reverse-transcribed total RNA or water as templates. After purification with a QIAquick PCR purification kit, PCR products were ligated into pCR 4Blunt-TOPO (Invitrogen) and transformed into One Shot Top10 Chemically Competent *E. coli* (Invitrogen). Sequencing was used to determine the presence of WT RPE65 and D477G RPE65 fragments (examples of sequence chromatograms from heterozygous KI animals are shown in Fig. 2C). To examine the ratio of WT RPE65 and D477G RPE65 mRNA, 95 cDNA clones from two heterozygous KI mice were randomly selected and sequenced.

SLO and OCT imaging

Mice were anesthetized by intraperitoneal injection of a cocktail consisting of 20 mg/ml ketamine and 1.75 mg/ml xylazine in phosphate-buffered saline at a dose of 0.1–0.13 ml per 25 g body weight. Pupils were dilated with 1% tropicamide (Henry Schein, Melville, NY) before imaging. Heidelberg Retinal Angiograph II (Heidelberg Engineering, Franklin, MA) was used for whole fundus imaging of retinas *in vivo*. Ultra-high resolution spectral domain OCT (Bioptigen, Morrisville, NC) was employed for imaging of retinas *in vivo*. Five frames of OCT images were acquired in the B-mode and then used to construct final averaged images. For quantitative measurements, the thickness of the ONL was measured 0.50 mm away from the optic nerve head in the superior, inferior, temporal and nasal retina. These values were then averaged.

ERG

Prior to recording, mice were dark adapted for 24 h. Under a safety light, mice were anesthetized by intraperitoneal injection of a cocktail consisting of 20 mg/ml ketamine and 1.75 mg/ml xylazine in phosphate-buffered saline at a dose of 0.1–0.13 ml per 25 g body weight. Pupils were dilated with 1% tropicamide (Henry Schein), and then 2.5% hypromellose was applied to keep the corneas hydrated. Contact lens electrodes were placed onto the corneas, and reference and ground electrodes were positioned subdermally between the ears and on the tail, respectively. All ERGs were recorded with the universal testing and electrophysiological system UTAS E-3000 (LKC Technologies, Gaithersburg, MD).

For single-flash scotopic ERG recording, the duration of white-light flash stimuli (from 20 μs to 1 ms) was adjusted to provide a range of illumination intensities from −3.7 to 2.3 log cd·s/m^2. For each intensity, 3 to 20 recordings were made at sufficient intervals between flash stimuli (from 3 to 90 s) to allow recovery from any photobleaching effects. The photopic ERG recordings were performed after bleaching at 1.4 log cd·s/m^2 for 10 minutes. For photopic ERG, the cone response was measured at four different light intensities (−0.7 to 2.3 log cd·s/m^2) in the presence of rod-desensitizing white-light background.

HPLC retinoid profiling

Eyes were enucleated from dark-adapted WT, heterozygous KI and homozygous KI mice and then homogenized in 10 mM sodium phosphate buffer, pH 8.0, containing 50% methanol (v/v) and 100 mM hydroxylamine. After 15 min of incubation at room temperature, 2 ml of 3 M sodium chloride was added. The resulting sample was extracted twice with 3 ml of ethyl acetate. Then, the combined organic phase was dried *in vacuo* and reconstituted in 400 μl of hexane. Extracted retinoids (100 μl) were separated on a normal phase HPLC column (Sil; 5 μm, 4.6 × 250 mm; Agilent Technologies) equilibrated with a stepwise gradient of 0.6% ethyl acetate in hexane at an isocratic flow rate of 1.4 ml/min for 17 min and 10% ethyl acetate in hexane at an isocratic flow rate of 1.4 ml/min for 25 min. Retinoids were detected by monitoring their absorbance at 325 nm and quantified based on correlations of their peak areas.

ACO/RPE65 chimera construct design

A chimeric ACO/RPE65 coding sequence was synthesized by replacing the nucleotides encoding residues 44–45, 431–442, 461 and 463 of *Synechocystis* ACO (GI: 81671293) with those encoding residues 36–37, 474–485, 506 and 508 of bovine RPE65 (GI: 27806125) (Genscript, Piscataway, NJ). The open reading frame was subcloned into the pET3a expression vector. The D434G point mutant (corresponding to D477G in RPE65 and referred to as such in the manuscript) was generated by the QuikChange site-directed mutagenesis protocol (Stratagene, San Diego, CA). Coding regions of all expression plasmids were verified by sequencing.

ACO/RPE65 chimera expression, purification and crystallization

ACO/RPE65 chimera and its D477G variant were expressed, purified and crystallized as described previously for ACO (36) with the following modifications. Protein expression was not chemically induced but instead relied on basal T7 promoter activity. Following purification, proteins were diluted into a buffer consisting of 20 mM HEPES-NaOH, pH 7 (Sigma-Aldrich) and 0.02% v/v Triton X-100 (Anatrace, Maumee, OH) to a final concentration of 10 mg/ml. Crystals were formed by the hanging-drop vapor diffusion method after mixing 2 μl drops of protein solution with 2 μl of a crystallant consisting of 0.1 M Bis–Tris propane, pH 6 (Sigma-Aldrich) and 21% w/v sodium polyacrylate 2100 (Molecular Dimensions, Maumee, OH). After 2–3 weeks of growth, crystals were cryoprotected in crystallant supplemented with 15% v/v ethylene glycol, flash cooled in liquid nitrogen and then stored in nitrogen vapor prior to X-ray exposure.

Diffraction data collection, structure solution and refinement

Diffraction data were collected at the NSLS II AMX and FMX beamlines or the APS NECAT IDE beamline. Data reduction was carried out with XDS (63). The ACO/RPE65 chimera structure, which was isomorphous to previous ACO structures (36,37), was solved by direct refinement in REFMAC (64) using the coordinates deposited under PDB accession code 4OU9 as a starting model. Amino acid replacements were performed with COOT (65). The ACO/RPE65 chimera coordinates were used as a search model to solve the structures of the two D477G crystal forms by molecular replacement in the program Phaser (66). Structural models were iteratively improved by manual real space refinement in COOT and reciprocal space refinement in REFMAC. Such models were periodically checked for geometric soundness and fit to the electron density maps with MOLPROBITY (67) and the wwPDB validation server (68).

Structure analysis

CCO amino acid sequence alignments were carried out with Clustal Omega (69) and were annotated with Espript (70). Structural motifs involving specific amino acid sequences were identified and analyzed with PDBeMotif using the MSDmotif algorithm (35). Secondary structures and contact surfaces for the ACO/RPE65 chimera crystal structures were analyzed with PDBsum (30) and PISA (71). Electrostatics calculations were carried out with APBS (72). Figures displaying three-dimensional structures were rendered using PyMOL (Schrödinger, LLC).

ACO/RPE65 chimera activity assays

Enzymatic activity of purified ACO and ACO/RPE65 proteins were assayed spectrophotometrically by monitoring formation of the all-*trans*-retinal product at 340 nm using all-*trans*-β-apo-8′-carotenol as the reaction substrate and assay conditions identical to those previously described (Supplementary Material, Fig. S3) (36).

Statistics

Data representing the means ± SEMs (unless otherwise indicated) are presented for results of at least three independent experiments. Significance between groups was determined either with the unpaired Student's *t*-test or one-way ANOVA with the Bonferroni post-test for comparisons of more than two groups. Sigma Plot 11.0 (Systat Software) was used to perform the statistical analyses.

Supplementary Material

Supplementary Material is available at *HMG* online.

Acknowledgements

We thank Dr. Leslie T. Webster Jr. (CWRU) for valuable comments on the manuscript. We thank Drs. Jianye Zhang, Lukas Hofmann and Marcin Golczak (CWRU) for sharing their expertise related to retinoid analysis and the RPE65 isomerization assay.

Conflict of Interest statement. None declared.

Funding

This research was supported in part by grants from the National Institutes of Health (EY009339 to K.P. and P.D.K., T32GM007250 to E.H.C and S.S, T32EY007157 to C.L.S, EY027283 and EY024864 to K.P. and core grants P30EY011373 and P30EY025585) and the Department of Veterans Affairs (IK2BX002683 to P.D.K). This work is based in part upon research conducted at the APS Northeastern Collaborative Access Team beamlines supported by grants GM103403, RR029205 and DE-AC02–06CH11357. Data for this study were measured at beamlines 17-ID-1 and 17-ID-2 of the National Synchrotron Light Source-II, which are supported by NIH grant GM111244 and the DOE Office of Biological and Environmental Research KP1605010. The NSLS-II is supported in part by the DOE Office of Science, Office of Basic Energy Sciences Program under contract number DE-SC0012704 (KC0401040). The Case Center for Synchrotron Biosciences is supported by NIH grant EB009998. K.P. is the John H. Hord Professor of Pharmacology.

References

1. Jin, M., Li, S., Moghrabi, W.N., Sun, H. and Travis, G.H. (2005) Rpe65 is the retinoid isomerase in bovine retinal pigment epithelium. *Cell*, **122**, 449–459.
2. Moiseyev, G., Chen, Y., Takahashi, Y., Wu, B.X. and Ma, J.X. (2005) RPE65 is the isomerohydrolase in the retinoid visual cycle. *Proc. Natl. Acad. Sci. U.S.A.*, **102**, 12413–12418.
3. Redmond, T.M., Poliakov, E., Yu, S., Tsai, J.Y., Lu, Z. and Gentleman, S. (2005) Mutation of key residues of RPE65 abolishes its enzymatic role as isomerohydrolase in the visual cycle. *Proc. Natl. Acad. Sci. U.S.A.*, **102**, 13658–13663.
4. Redmond, T.M., Yu, S., Lee, E., Bok, D., Hamasaki, D., Chen, N., Goletz, P., Ma, J.X., Crouch, R.K. and Pfeifer, K. (1998) Rpe65 is necessary for production of 11-cis-vitamin A in the retinal visual cycle. *Nat. Genet.*, **20**, 344–351.
5. Nicoletti, A., Wong, D.J., Kawase, K., Gibson, L.H., Yang-Feng, T.L., Richards, J.E. and Thompson, D.A. (1995) Molecular characterization of the human gene encoding an abundant 61 kDa protein specific to the retinal pigment epithelium. *Hum. Mol. Genet.*, **4**, 641–649.
6. Schwartz, S.H., Tan, B.C., Gage, D.A., Zeevaart, J.A. and McCarty, D.R. (1997) Specific oxidative cleavage of carotenoids by VP14 of maize. *Science*, **276**, 1872–1874.
7. Hamel, C.P., Tsilou, E., Pfeffer, B.A., Hooks, J.J., Detrick, B. and Redmond, T.M. (1993) Molecular cloning and expression of RPE65, a novel retinal pigment epithelium-specific microsomal protein that is post-transcriptionally regulated in vitro. *J. Biol. Chem.*, **268**, 15751–15757.
8. Chacon-Camacho, O.F. and Zenteno, J.C. (2015) Review and update on the molecular basis of Leber congenital amaurosis. *World J. Clin. Cases*, **3**, 112–124.
9. Bowne, S.J., Humphries, M.M., Sullivan, L.S., Kenna, P.F., Tam, L.C., Kiang, A.S., Campbell, M., Weinstock, G.M., Koboldt, D.C. and Ding, L. (2011) A dominant mutation in RPE65 identified by whole-exome sequencing causes retinitis pigmentosa with choroidal involvement. *Eur. J. Hum. Genet.*, **19**, 1074–1081.
10. Hull, S., Mukherjee, R., Holder, G.E., Moore, A.T. and Webster, A.R. (2016) The clinical features of retinal disease due to a dominant mutation in RPE65. *Mol. Vis.*, **22**, 626–635.
11. Shin, Y., Moiseyev, G., Chakraborty, D. and Ma, J.X. (2017) A dominant mutation in Rpe65, D477G, delays dark adaptation and disturbs the visual cycle in the mutant knock-in mice. *Am. J. Pathol.*, **187**, 517–527.
12. Wilson, J.H. and Wensel, T.G. (2003) The nature of dominant mutations of rhodopsin and implications for gene therapy. *Mol. Neurobiol.*, **28**, 149–158.
13. Bereta, G., Kiser, P.D., Golczak, M., Sun, W., Heon, E., Saperstein, D.A. and Palczewski, K. (2008) Impact of retinal disease-associated RPE65 mutations on retinoid isomerization. *Biochemistry*, **47**, 9856–9865.
14. Takahashi, Y., Chen, Y., Moiseyev, G. and Ma, J.X. (2006) Two point mutations of RPE65 from patients with retinal dystrophies decrease the stability of RPE65 protein and abolish its isomerohydrolase activity. *J. Biol. Chem.*, **281**, 21820–21826.
15. Bavik, C.O., Busch, C. and Eriksson, U. (1992) Characterization of a plasma retinol-binding protein membrane receptor expressed in the retinal pigment epithelium. *J. Biol. Chem.*, **267**, 23035–23042.
16. Li, S., Izumi, T., Hu, J., Jin, H.H., Siddiqui, A.A., Jacobson, S.G., Bok, D. and Jin, M. (2014) Rescue of enzymatic function for

disease-associated RPE65 proteins containing various missense mutations in non-active sites. *J. Biol. Chem.*, **289**, 18943–18956.
17. Li, S.H., Izumi, T., Hu, J., Jin, H.H., Siddiqui, A.A.A., Jacobson, S.G., Bok, D. and Jin, M.H. (2014) Rescue of enzymatic function for disease-associated RPE65 proteins containing various missense mutations in non-active sites. *J. Biol. Chem.*, **289**, 18943–18956.
18. Li, S., Hu, J., Jin, R.J., Aiyar, A., Jacobson, S.G., Bok, D. and Jin, M. (2015) Temperature-sensitive retinoid isomerase activity of RPE65 mutants associated with Leber congenital amaurosis. *J. Biochem.*, **158**, 115–125.
19. Li, S., Samardzija, M., Yang, Z., Grimm, C. and Jin, M. (2016) Pharmacological amelioration of cone survival and vision in a mouse model for Leber congenital amaurosis. *J. Neurosci.*, **36**, 5808–5819.
20. Maeda, A., Okano, K., Park, P.S., Lem, J., Crouch, R.K., Maeda, T. and Palczewski, K. (2010) Palmitoylation stabilizes unliganded rod opsin. *Proc. Natl. Acad. Sci. U.S.A.*, **107**, 8428–8433.
21. Mustafi, D., Maeda, T., Kohno, H., Nadeau, J.H. and Palczewski, K. (2012) Inflammatory priming predisposes mice to age-related retinal degeneration. *J. Clin. Invest.*, **122**, 2989–3001.
22. Zhang, N., Kolesnikov, A.V., Jastrzebska, B., Mustafi, D., Sawada, O., Maeda, T., Genoud, C., Engel, A., Kefalov, V.J. and Palczewski, K. (2013) Autosomal recessive retinitis pigmentosa E150K opsin mice exhibit photoreceptor disorganization. *J. Clin. Invest.*, **123**, 121–137.
23. Chen, Y., Palczewska, G., Masuho, I., Gao, S., Jin, H., Dong, Z., Gieser, L., Brooks, M.J., Kiser, P.D., Kern, T.S. *et al.* (2016) Synergistically acting agonists and antagonists of G protein-coupled receptors prevent photoreceptor cell degeneration. *Sci. Signal.*, **9**, ra74.
24. Samardzija, M., von Lintig, J., Tanimoto, N., Oberhauser, V., Thiersch, M., Reme, C.E., Seeliger, M., Grimm, C. and Wenzel, A. (2007) R91W mutation in Rpe65 leads to milder early-onset retinal dystrophy due to the generation of low levels of 11-cis-retinal. *Hum. Mol. Genet.*, **17**, 281–292.
25. Redmond, T.M., Weber, C.H., Poliakov, E., Yu, S. and Gentleman, S. (2007) Effect of Leu/Met variation at residue 450 on isomerase activity and protein expression of RPE65 and its modulation by variation at other residues. *Mol. Vis.*, **13**, 1813–1821.
26. Imanishi, Y., Batten, M.L., Piston, D.W., Baehr, W. and Palczewski, K. (2004) Noninvasive two-photon imaging reveals retinyl ester storage structures in the eye. *J. Cell Biol.*, **164**, 373–383.
27. Imanishi, Y., Gerke, V. and Palczewski, K. (2004) Retinosomes: new insights into intracellular managing of hydrophobic substances in lipid bodies. *J. Cell Biol.*, **166**, 447–453.
28. Sheridan, C., Boyer, N.P., Crouch, R.K. and Koutalos, Y. (2017) RPE65 and the accumulation of retinyl esters in mouse retinal pigment epithelium. *Photochem. Photobiol.*, **93**, 844–848.
29. Lek, M., Karczewski, K.J., Minikel, E.V., Samocha, K.E., Banks, E., Fennell, T., O'Donnell-Luria, A.H., Ware, J.S., Hill, A.J., Cummings, B.B. *et al.* (2016) Analysis of protein-coding genetic variation in 60, 706 humans. *Nature*, **536**, 285–291.
30. Laskowski, R.A., Jabłońska, J., Pravda, L., Vařeková, R.S. and Thornton, J.M. (2018) PDBsum: structural summaries of PDB entries. *Protein Sci.*, **27**, 129–134.
31. Kiser, P.D., Golczak, M., Lodowski, D.T., Chance, M.R. and Palczewski, K. (2009) Crystal structure of native RPE65, the retinoid isomerase of the visual cycle. *Proc. Natl. Acad. Sci. U.S.A.*, **106**, 17325–17330.
32. Kiser, P.D., Farquhar, E.R., Shi, W., Sui, X., Chance, M.R. and Palczewski, K. (2012) Structure of RPE65 isomerase in a lipidic matrix reveals roles for phospholipids and iron in catalysis. *Proc. Natl. Acad. Sci. U.S.A.*, **109**, E2747–E2756.
33. Richardson, J.S. (1981) The anatomy and taxonomy of protein structure. *Adv. Protein Chem.*, **34**, 167–339.
34. Hutchinson, E.G. and Thornton, J.M. (1994) A revised set of potentials for beta-turn formation in proteins. *Protein Sci.*, **3**, 2207–2216.
35. Golovin, A. and Henrick, K. (2008) MSDmotif: exploring protein sites and motifs. *BMC Bioinform.*, **9**, 312.
36. Sui, X., Kiser, P.D., Che, T., Carey, P.R., Golczak, M., Shi, W., von Lintig, J. and Palczewski, K. (2014) Analysis of carotenoid isomerase activity in a prototypical carotenoid cleavage enzyme, apocarotenoid oxygenase (ACO). *J. Biol. Chem.*, **289**, 12286–12299.
37. Kloer, D.P., Ruch, S., Al-Babili, S., Beyer, P. and Schulz, G.E. (2005) The structure of a retinal-forming carotenoid oxygenase. *Science*, **308**, 267–269.
38. Cideciyan, A.V. (2010) Leber congenital amaurosis due to RPE65 mutations and its treatment with gene therapy. *Prog. Retin. Eye Res.*, **29**, 398–427.
39. Laney, J.D. and Hochstrasser, M. (1999) Substrate targeting in the ubiquitin system. *Cell*, **97**, 427–430.
40. Wilkie, A.O. (1994) The molecular basis of genetic dominance. *J. Med. Genet.*, **31**, 89–98.
41. Felius, J., Thompson, D.A., Khan, N.W., Bingham, E.L., Jamison, J.A., Kemp, J.A. and Sieving, P.A. (2002) Clinical course and visual function in a family with mutations in the RPE65 gene. *Arch. Ophthalmol.*, **120**, 55–61.
42. Poehner, W.J., Fossarello, M., Rapoport, A.L., Aleman, T.S., Cideciyan, A.V., Jacobson, S.G., Wright, A.F., Danciger, M. and Farber, D.B. (2000) A homozygous deletion in RPE65 in a small Sardinian family with autosomal recessive retinal dystrophy. *Mol. Vis.*, **6**, 192–198.
43. Yzer, S., van den Born, L.I., Schuil, J., Kroes, H.Y., van Genderen, M.M., Boonstra, F.N., van den Helm, B., Brunner, H.G., Koenekoop, R.K. and Cremers, F.P. (2003) A Tyr368His RPE65 founder mutation is associated with variable expression and progression of early onset retinal dystrophy in 10 families of a genetically isolated population. *J. Med. Genet.*, **40**, 709–713.
44. Morimura, H., Fishman, G.A., Grover, S.A., Fulton, A.B., Berson, E.L. and Dryja, T.P. (1998) Mutations in the RPE65 gene in patients with autosomal recessive retinitis pigmentosa or Leber congenital amaurosis. *Proc. Natl. Acad. Sci. U.S.A.*, **95**, 3088–3093.
45. Strauss, O. (2005) The retinal pigment epithelium in visual function. *Physiol. Rev.*, **85**, 845–881.
46. Aguzzi, A. and O'Connor, T. (2010) Protein aggregation diseases: pathogenicity and therapeutic perspectives. *Nat. Rev. Drug Discov.*, **9**, 237–248.
47. Rousseau, F., Schymkowitz, J. and Serrano, L. (2006) Protein aggregation and amyloidosis: confusion of the kinds? *Curr. Opin. Struct. Biol.*, **16**, 118–126.
48. De Baets, G., Van Doorn, L., Rousseau, F. and Schymkowitz, J. (2015) Increased aggregation is more frequently associated to human disease-associated mutations than to neutral polymorphisms. *PLoS Comput. Biol.*, **11**, e1004374.

49. Reumers, J., Maurer-Stroh, S., Schymkowitz, J. and Rousseau, F. (2009) Protein sequences encode safeguards against aggregation. *Hum. Mutat.*, **30**, 431–437.
50. Monplaisir, N., Merault, G., Poyart, C., Rhoda, M.D., Craescu, C., Vidaud, M., Galacteros, F., Blouquit, Y. and Rosa, J. (1986) Hemoglobin-S antilles - a variant with lower solubility than hemoglobin-S and producing sickle-cell disease in heterozygotes. *Proc. Natl. Acad. Sci. U.S.A.*, **83**, 9363–9367.
51. Harrington, D.J., Adachi, K. and Royer, W.E. (1997) The high resolution crystal structure of deoxyhemoglobin S. *J. Mol. Biol.*, **272**, 398–407.
52. Tripette, J., Loko, G., Samb, A., Gogh, B.D., Sewade, E., Seck, D., Hue, O., Romana, M., Diop, S., Diaw, M. *et al.* (2010) Effects of hydration and dehydration on blood rheology in sickle cell trait carriers during exercise. *Am. J. Physiol. Heart Circ. Physiol.*, **299**, H908–H914.
53. Kark, J.A., Posey, D.M., Schumacher, H.R. and Ruehle, C.J. (1987) Sickle-cell trait as a risk factor for sudden death in physical training. *N. Engl. J. Med.*, **317**, 781–787.
54. Anzalone, M.L., Green, V.S., Buja, M., Sanchez, L.A., Harrykissoon, R.I. and Eichner, E.R. (2010) Sickle cell trait and fatal rhabdomyolysis in football training: a case study. *Med. Sci. Sports Exerc.*, **42**, 3–7.
55. Kmoch, S., Brynda, J., Asfaw, B., Bezouska, K., Novak, P., Rezacova, P., Ondrova, L., Filipec, M., Sedlacek, J. and Elleder, M. (2000) Link between a novel human gammaD-crystallin allele and a unique cataract phenotype explained by protein crystallography. *Hum. Mol. Genet.*, **9**, 1779–1786.
56. Pande, A., Pande, J., Asherie, N., Lomakin, A., Ogun, O., King, J. and Benedek, G.B. (2001) Crystal cataracts: human genetic cataract caused by protein crystallization. *Proc. Natl. Acad. Sci. U.S.A.*, **98**, 6116–6120.
57. Mattapallil, M.J., Wawrousek, E.F., Chan, C.C., Zhao, H., Roychoudhury, J., Ferguson, T.A. and Caspi, R.R. (2012) The Rd8 mutation of the Crb1 gene is present in vendor lines of C57BL/6N mice and embryonic stem cells, and confounds ocular induced mutant phenotypes. *Invest. Ophthalmol. Vis. Sci.*, **53**, 2921–2927.
58. Chelstowska, S., Widjaja-Adhi, M.A.K., Silvaroli, J.A. and Golczak, M. (2017) Impact of LCA-associated E14L LRAT mutation on protein stability and retinoid homeostasis. *Biochemistry*, **56**, 4489–4499.
59. Kitamura, T., Koshino, Y., Shibata, F., Oki, T., Nakajima, H., Nosaka, T. and Kumagai, H. (2003) Retrovirus-mediated gene transfer and expression cloning: powerful tools in functional genomics. *Exp. Hematol.*, **31**, 1007–1014.
60. Wei, H., Xun, Z., Granado, H., Wu, A. and Handa, J.T. (2016) An easy, rapid method to isolate RPE cell protein from the mouse eye. *Exp. Eye Res.*, **145**, 450–455.
61. Golczak, M., Kiser, P.D., Lodowski, D.T., Maeda, A. and Palczewski, K. (2010) Importance of membrane structural integrity for RPE65 retinoid isomerization activity. *J. Biol. Chem.*, **285**, 9667–9682.
62. Xin-Zhao Wang, C., Zhang, K., Aredo, B., Lu, H. and Ufret-Vincenty, R.L. (2012) Novel method for the rapid isolation of RPE cells specifically for RNA extraction and analysis. *Exp. Eye Res.*, **102**, 1–9.
63. Kabsch, W. (2010) XDS. *Acta Crystallogr. D*, **66**, 125–132.
64. Murshudov, G.N., Skubak, P., Lebedev, A.A., Pannu, N.S., Steiner, R.A., Nicholls, R.A., Winn, M.D., Long, F. and Vagin, A.A. (2011) REFMAC5 for the refinement of macromolecular crystal structures. *Acta Crystallogr. D*, **67**, 355–367.
65. Emsley, P., Lohkamp, B., Scott, W.G. and Cowtan, K. (2010) Features and development of Coot. *Acta Crystallogr. D*, **66**, 486–501.
66. McCoy, A.J., Grosse-Kunstleve, R.W., Adams, P.D., Winn, M.D., Storoni, L.C. and Read, R.J. (2007) Phaser crystallographic software. *J. Appl. Crystallogr*, **40**, 658–674.
67. Chen, V.B., Arendall, W.B., 3rd, Headd, J.J., Keedy, D.A., Immormino, R.M., Kapral, G.J., Murray, L.W., Richardson, J.S. and Richardson, D.C. (2010) MolProbity: all-atom structure validation for macromolecular crystallography. *Acta Crystallogr. D*, **66**, 12–21.
68. Read, R.J., Adams, P.D., Arendall, W.B., 3rd, Brunger, A.T., Emsley, P., Joosten, R.P., Kleywegt, G.J., Krissinel, E.B., Lutteke, T., Otwinowski, Z. *et al.* (2011) A new generation of crystallographic validation tools for the protein data bank. *Structure*, **19**, 1395–1412.
69. Sievers, F., Wilm, A., Dineen, D., Gibson, T.J., Karplus, K., Li, W., Lopez, R., McWilliam, H., Remmert, M., Soding, J. *et al.* (2014) Fast, scalable generation of high-quality protein multiple sequence alignments using Clustal Omega. *Mol. Syst. Biol.*, **7**, 539.
70. Robert, X. and Gouet, P. (2014) Deciphering key features in protein structures with the new ENDscript server. *Nucleic Acids Res.*, **42**, W320–W324.
71. Krissinel, E. and Henrick, K. (2007) Inference of macromolecular assemblies from crystalline state. *J. Mol. Biol.*, **372**, 774–797.
72. Baker, N.A., Sept, D., Joseph, S., Holst, M.J. and McCammon, J.A. (2001) Electrostatics of nanosystems: application to microtubules and the ribosome. *Proc. Natl. Acad. Sci. U.S.A.*, **98**, 10037–10041.